

**“An Approximate Kalman Filter for
Ocean Data Assimilation;
An Example with an Idealized Gulf Stream Model”**

by

Ichiro Fukunori

Jet Propulsion Laboratory, California Institute of Technology,
4800 Oak Grove Drive, Pasadena CA 91109

and

Paola Malanotte-Rizzoli

Department of Earth Atmospheric and Planetary Sciences,
Massachusetts Institute of Technology,
77 Massachusetts Avenue, Cambridge MA 02139

Accepted for publication
Journal of Geophysical Research

FINAL VERSION

November 14, 1994

Abstract

A practical method of data assimilation for use with large, nonlinear, ocean general circulation models is explored. A Kalman filter based on approximations of the state error covariance matrix is presented, employing a reduction of the effective model dimension, the error's asymptotic steady-state limit, and a time-invariant linearization of the dynamic model for the error integration. The approximations lead to dramatic computational savings in applying estimation theory to large complex systems. We examine the utility of the approximate filter in assimilating different measurement types using a twin experiment of an idealized Gulf Stream. A nonlinear primitive equation model of an unstable east-west jet is studied with a state dimension exceeding 170,000 elements. Assimilation of various pseudo measurements are examined, including velocity, density, and volume transport at localized arrays, and realistic distributions of satellite altimetry and acoustic tomography observations. Results are compared in terms of their effects on the accuracies of the estimation. The approximate filter is shown to outperform a previous study that used an empirical nudging scheme. The examples demonstrate that useful approximate estimation errors can be computed in a practical manner for general circulation models.

1. Introduction

Estimating the state of the ocean circulation is one of the central issues in oceanography. Traditionally, such studies have been pursued by two separate approaches; inductive analyses of direct observations on the one hand and deductive studies through theoretical modeling based on first principles on the other. A systematic approach to the former includes inverse modeling (e.g., Martel and Wunsch, 1993), and the latter is represented by numerical simulations using general circulation models (e.g., Semtner and Chervin, 1992). Most recently, the issue of combining the two approaches, namely data assimilation, has received increasing attention, due primarily to the increased amount of available observations. These include both data from satellites (e.g., GEOSAT, ERS-1, TOPEX/POSEIDON) and in situ observational experiments (e.g., WOCE, TOGA, SYNOP). Data assimilation is a combination of data analysis and numerical modeling, so as to make optimal use of the information content of the former and the theoretical knowledge of the latter, which together compensate their respective limitations. Inverse modeling has now reached a stage that simple steady-state kinematic and geostrophic constraints cannot fully account for all observations, but requires use of models with more physics. On the other hand, numerical simulations suffer from inaccuracies in the external forcing, boundary and initial conditions, and model physics including effects of subgrid-scale processes.

The purpose of the present study is two-fold. The primary objective is to explore a method that allows near-optimal but efficient assimilation with formal error estimates using complete general circulation models. The other goal is to explore assimilation of various data types and to compare them with results obtained by nudging, which is a simpler assimilation method. The data types considered here are direct point-wise measurements of velocity, density, and volume transport at localized arrays, and indirect non-traditional measurements from satellite altimetry and acoustic tomography.

Conceptually, data assimilation modifies model variables according to what is measured and what the model physics require. Various procedures have been explored for ocean data assimilation, which might be roughly divided into two categories. In one, data are assimilated into comparatively complex dynamical models in an ad hoc scheme designed to “nudge” the model toward the data. Examples include nudging (e.g., Malanotte-Rizzoli and Holland, 1986) and various forms of optimal interpolation (e.g., Robinson et al., 1989). Another class is based on formal estimation and control

theory that minimizes the data-model misfit under the constraint of the model dynamics. These objective approaches include the adjoint method (e.g., Marotzke and Wunsch, 1993) and Kalman filtering and smoothing (e.g., Fukumori et al., 1993).

The former class of methods lack accounting for errors in the data and model, and could conceivably introduce more errors into the model estimate than information from the data, due to statistical and dynamic inconsistencies. The latter class, on the other hand, involve formidable computational requirements, such that in general, applications have been limited to simple models with less physics and/or model resolution than typical numerical simulations. The adjoint method is generally more efficient than Kalman filtering and smoothing, but nevertheless, involves an order of magnitude more iterations by the forward model and its adjoint than simulations. The efficiency of the adjoint method is attained at the expense of the absence of formal error estimates, and explicit error derivations would render the computational cost comparable to those of Kalman filtering and smoothing.

Thus, there is a gap between the two classes of approaches in combining data with models. A trade-off exists between optimality with formal error estimates and complexity of the numerical models that are used. Fukumori et al. (1993) explored an approximate Kalman filter and smoother based on an asymptotic time-invariant error limit, which significantly reduces the computational requirements of estimation theory. However, their model, although a primitive equation model, was still much too simplified to be useful due primarily to the coarse resolution and to a lesser extent the linearized dynamics. What follows is in part an extension of the work by Fukumori et al. (1993) in applying Kalman filtering to a model with a much finer resolution, and thus larger state dimension, and to one that also includes nonlinear dynamics. Approximations will be introduced that reduce the filter's effective dimension and simplify the state's error integration. It should be emphasized that the objective of these simplifications is to derive an *approximate* filter for data assimilation, and is *not* meant to replace or to simplify the dynamic model per se.

Perhaps the most studied observing system in the context of ocean data assimilation is that by satellite altimetry [e.g., Marshall, 1985; Robinson and Leslie, 1985; Kindle, 1986; Holland and Malanotte-Rizzoli, 1989; White et al., 1990a, b, c; Mellor and Ezer, 1991; Fukumori et al., 1993]. The attention to altimetry studies is primarily

due to the satellites' global and continuous coverage and the associated large number of observations that provide stringent constraints on the estimation.

In contrast, traditional oceanographic datasets have received, until now, relatively little attention in assimilation studies. Thus far, very few papers have addressed the issue of assimilating localized oceanographic measurements and of assessing their effectiveness in constraining a dynamical model. Idealized assimilations of hydrographic surveys were carried out by Malanotte-Rizzoli and Holland (1986, 1988) and Malanotte-Rizzoli et al. (1989). Sparse expandable bathythermographs (XBT) and infrared satellite imagery (IR) were used for feature models of the Gulf Stream system by Robinson et al. (1989) and Robinson (1992) in the Harvard Gulfcast effort. In the equatorial ocean, XBTs were used by Moore and Anderson (1989), and tide gauge measurements were assimilated in the studies of Miller and Cane (1989) and of Smedstad and O'Brien (1991). The study of Malanotte-Rizzoli and Young (1992) addressed the specific question; can traditional measurements taken at localized arrays of moorings be effective when assimilated into an ocean circulation model? They used a model of the Gulf Stream focusing on process studies, specifically aimed at reconstructing the system behavior of a jet's meander evolution from limited point-wise measurements.

Assimilation of acoustic tomography measurements has received even less attention than other in situ measurements. Sheinbaum (1989) conducted simulations of tomographic assimilation using a simple one-layer model. Tomography can provide unique continuous synoptic observations of the three-dimensional interior density and velocity field, which are not directly accessible by the surface measurements from satellites nor by traditional in situ measurements that are sparse.

One of the ultimate goals of estimation is to combine all observations into a single coherent model of the ocean. In this manuscript, we will take some steps towards this objective and explore the problem of assimilating various types of observations discussed above into a realistic model of the ocean. One of the major issues raised in data assimilation is how information from observations are propagated within the model, spatially, temporally, and among different properties. This is especially an issue with non-traditional measurements that do not provide direct observations of the model's prognostic variables, such as altimetry and tomography. Among the advantages of estimation theory, Kalman filtering does not distinguish between observations of individual prognostic variables and diagnostic quantities, and it will be straightforward

to assimilate altimetric or tomographic measurements as is to analyze velocity or density data.

The present study is based on the twin experiment employed in the analysis of Malanotte-Rizzoli and Young (1992; hereafter referred to as RY92) of an idealized model of the Gulf Stream. The motivation for RY92 was provided by the SYNoptic Ocean Prediction (SYNOP) experiment carried out in the period 1987--1990 in the Gulf Stream system (Fig 1). The model configuration of RY92 was idealized, with the SYNOP arrays schematized as two identical arrays in a rectangular domain (Fig 2). The model is of an unstable jet, based on a non-linear, three-dimensional, primitive equation, general circulation model, and they used a nudging scheme for the assimilation. We will revisit the question of the effectiveness of localized datasets in constraining a dynamical model with the approximate Kalman filter using this same numerical model as RY92. One of the objectives of the present analysis is to assess the efficacy of a suboptimal Kalman filter versus nudging when performing identical assimilation experiments. This is an ambitious application of estimation theory, involving issues of the model's large dimension, nonlinearity, instabilities, and of the complex algorithm of the model itself.

This paper is organized as follows. In section 2.1 we briefly review some of the issues of Kalman filtering, and introduce the reduced-order, static, linearized filter in section 2.2. In section 3, we discuss results from the assimilation experiments. Sections 3.1 and 3.2 are devoted to describing the strategies that were taken in constructing the approximate Kalman filter for the particular example; 3.1 discusses the coarse state approximation and linearization and 3.2 describes the choice for the data error and model process noise used in deriving the filter. In section 3.3 we revisit the assimilation of localized cluster datasets examined by RY92 but using the approximate Kalman filter, while the examples of assimilating the less traditional measurements (altimetry and tomography) are discussed in section 3.4. In section 4, Summary and Discussion, we present our conclusions and describe directions for future research.

2. Approximate Kalman Filter

In this section we describe a method of data assimilation based on an approximate form of the Kalman filter. The approximation is a linearized Kalman filter that combines use of a static estimation error covariance matrix (Fukumori et al., 1993) and a method

of reducing the model's effective state dimension. First, we briefly review the issues of Kalman filtering and the static approximation.

2.1 Review of Some Issues

The Kalman filter is essentially a recursive least-squares inversion of observations for model variables, using a dynamic model as a constraint. The Kalman filter performs a weighted average of model estimate and data, where the weights are based on the relative accuracies of the two. The result is an improved estimate of model variables, where the improvement is achieved in a statistical sense; the result has the least expected error given the measurements and the model, along with their error statistics. For example, let there be, at time t , a model estimate $\mathbf{x}(t, -)$, where the minus sign denotes a model prediction, and a set of observations $\mathbf{y}(t)$, with corresponding independent error covariance matrix estimates $\mathbf{P}(t, -)$ and $\mathbf{R}(t)$, respectively. Estimation theory (e.g., Gelb, 1974) states that the optimal combination of the model, \mathbf{x} , and observation, \mathbf{y} , is given by (regardless of the model being linear or nonlinear),

$$\mathbf{x}(t) = \mathbf{x}(t, -) + \mathbf{K}(t)[\mathbf{y}(t) - \mathbf{H}\mathbf{x}(t, -)] \quad (1)$$

where the weight \mathbf{K} (Kalman gain) is,

$$\mathbf{K}(t) = \mathbf{P}(t, -)\mathbf{H}^T[\mathbf{H}\mathbf{P}(t, -)\mathbf{H}^T + \mathbf{R}]^{-1} \quad (2)$$

Bold lower and upper case characters denote vectors and matrices, respectively. \mathbf{H} is a matrix such that $\mathbf{H}\mathbf{x}$ is the model's theoretical estimate of what is observed. (Note that this formalism does not distinguish observations being either functions of prognostic or diagnostic model variables.) The improved estimate, $\mathbf{x}(t)$, is then time-stepped by the model until another set of measurements are available and the assimilation is repeated. For a recent review of the Kalman filter and its applications in meteorology and oceanography, see Ghil and Malanotte-Rizzoli (1991).

Although theoretically straightforward, practical difficulties arise in applying the Kalman filter to oceanic data assimilation. The difficulty is in integrating the state's error covariance matrix, \mathbf{P} , in time, which makes up the Kalman gain (\mathbf{K} , Eq 2) that performs the least-squares averaging (Eq 1). The error covariance matrix evolves in time (Riccati equation) according to the model dynamics, just as the model state itself does. Integrating each column of the matrix is computationally equivalent to

integrating the model state (numerical simulations). But since there are as many columns in the matrix as there are independent variables (model state), the Riccati equation requires the-size-of-the-model times larger computational resources (storage and CPU time) than simulations. For example, a primitive equation model with a modest grid dimension of $100 \times 100 \times 10$ would have a model state size of 3×10^5 (three variables on each grid point). The storage requirement of integrating the covariance matrix would be at least 3×10^5 larger and computational time 6×10^5 longer than integrating just the set of 3×10^5 model variables. (The additional factor of two in computational time arises because the covariance is a second order moment.) A simulation of such a model that would require, for example, 0.3 Mw memory and 1 CPU hour would require 90 GW (!) memory and 68.5 CPU YEARS (!) to compute the corresponding evolution of the error covariance matrix. Therefore, direct application of Kalman filters to oceanic data assimilation will be limited to simple models that have small state dimensions for the foreseeable future, even with the anticipated teraflop massively parallel supercomputers.

On the other hand, the essence of Kalman filtering is in the weights, \mathbf{P} , and by deriving and using an approximate error estimate, the most costly step of Kalman filtering can be simplified. One such approximation is the use of a static asymptotic limit of the model error covariance matrix in place of the time-evolving error estimate (Fukumori et al., 1993). Under certain circumstances, the Riccati equation converges exponentially fast to a unique solution that results in a time-invariant filter (Anderson and Moore, 1979). The steady-state approximation substantially reduces the amount of computation (CPU time) in Kalman filtering by eliminating the continuous time-integration of the model error covariance, \mathbf{P} . In the example of Fu et al. (1993), a full Kalman filter for an equatorial wave model required 4200 CPU seconds whereas the asymptotic approximation required a mere 170 seconds. At the same time, the differences between the two estimates were statistically indistinguishable, despite the system being time-varying which violates the strict existence criteria of the asymptotic error limit (Goodwin and Sin, 1984). However, the matrices involved in the static error estimate calculation have the same dimension as the full Kalman filter, and subsequently the computational requirements would still be formidable for large models. For example, derivation of the asymptotic filter for the $100 \times 100 \times 10$ example above would still require 90 G W memory, and although reduced by one to two orders of magnitude, the

CPU time requirement would remain enormous (≈ 6 CPU months as opposed to 68.5 CPU years). Therefore, the steady-state approximation alone will not make Kalman filtering feasible for the general oceanic problem.

In the next section, we describe another approximation which reduces the effective dimension of the matrices involved, and with it, the storage and computational requirements of Kalman filtering. We emphasize again that the objective of the simplifications is solely to compute an approximate model error covariance matrix \mathbf{P} and replace that in Eqs (1, 2) for data assimilation, and is not to replace the numerical model itself.

2.2 Reduced-Order, Static, Linearized Kalman Filter

The grid size of a model and the resulting dimensionality of the model state is often dictated by numerical accuracy and stability rather than by physical constraint, and the most energetic scales in model simulations are much larger than the smallest grid spacing. On the other hand, considering the sparseness of even the most extensive oceanographic measurements (e.g., WOCE and TO PEX), the sampling theorem would suggest that most of the information directly available from data are at the large spatial scales. Then, one might consider limiting the analysis by assimilation to the large spatial scales, and thereby effectively reducing the dimensionality of the problem. For example, one might directly assimilate the large spatial scale information from the measurements into the model, rather than attempting to correct all scales simultaneously. Although such an approximation would no longer be formally optimal, given the typical red oceanic spectra, the degradation may be minimal. Furthermore, the errors incurred by such an approximation may be of second order at present, given our crude understanding about the accuracies of model simulations themselves and those of the observing systems. The idea is to approximate the model error covariance with one that has fewer degrees of freedom. Bennett and Budgell (1987) have examined such a limit in terms of assuring regularity of the estimation. Such a state dimension reduction scheme can be formulated mathematically for general models and observations.

Assume there exists some approximation, $\mathbf{x}'(t)$, of the original model state ($\mathbf{x}(t)$) with a smaller dimension,

$$\mathbf{x}(t) - \bar{\mathbf{x}} \approx \mathbf{I} \setminus \mathbf{X}'(t) \quad (3)$$

The approximation is defined, without loss of generality, around some prescribed time-invariant reference state, $\bar{\mathbf{x}}$, in anticipation of linearizing nonlinear models around such

a reference. Matrix B is the transformation matrix defining the approximation. One could think of the subspace defined by B as the low wavenumber components of the model spectra, or simply values of the model on a coarse grid. Given such a relationship, we can approximate the statistical properties of $\mathbf{x}(t)$ by those of $\mathbf{x}'(t)$. For example, given (3), the error covariance of $\mathbf{x}(t)$ ($\mathbf{P}(t)$) maybe approximated by the error of $\mathbf{x}'(t)$ ($\mathbf{P}'(t)$) by,

$$\mathbf{P}(t) \approx \mathbf{B}\mathbf{P}'(t)\mathbf{B}^T \quad (4)$$

which can be substituted into the Kalman *gain* (Eq 2) for assimilation. Note that, since $\bar{\mathbf{x}}$ is a prescribed value, it has no error and is statistically inconsequential. Given the smaller dimension, derivation of the statistical properties of the 'coarse' state $\mathbf{x}'(t)$ will be computationally less demanding than that for the original model, $\mathbf{x}(t)$. The dynamical equations for $\mathbf{x}'(t)$ may be constructed by directly combining the transformation B with the original model for $\mathbf{x}(t)$, and is described below.

Equation (3) is an approximation and the exact relationship involves the null space of the transformation;

$$\mathbf{x}(t) - \bar{\mathbf{x}} = \mathbf{B}\mathbf{x}'(t) + \mathbf{U}\mathbf{c}(t) \quad (5)$$

Here, matrix \mathbf{U} spans the null space of the columns of B , and $\mathbf{c}(t)$ is its amplitudes. Defining the pseudo inverse of B as B^* , we may invert Eq (5) and get,

$$\mathbf{B}^*(\mathbf{x}(t) - \bar{\mathbf{x}}) = \mathbf{x}'(t) \quad (6)$$

which is an identity that defines the coarse state, $\mathbf{x}'(t)$. Being a pseudo inverse, note that in general,

$$\mathbf{B}^*\mathbf{B} = \mathbf{I} \quad (7)$$

(where \mathbf{I} is the identity matrix) but that,

$$\mathbf{B}\mathbf{B}^* \neq \mathbf{I} \quad (8)$$

Denote the original dynamic model by a vector function \mathcal{F} , which describes the time evolution of the model state, $\mathbf{x}(t)$;

$$\mathbf{x}(t+1) = \mathcal{F}(\mathbf{x}(t), \mathbf{w}(t)) \quad (9)$$

where $\mathbf{w}(t)$ denotes the various forces and boundary conditions. The observations, $\mathbf{y}(t)$, can be theoretically related to the model state by another function \mathcal{E} ,

$$\mathbf{y}(t) = \mathcal{E}(\mathbf{x}(t)) + \mathbf{n} \quad (10)$$

where \mathbf{n} is the observation error. (Time index for \mathbf{n} and other error terms below are dropped for notational simplicity.) We may directly obtain equivalent equations for the reduced state, $\mathbf{x}'(t)$, by substituting Eqs (5, 6) into Eqs (9, 10);

$$\mathbf{x}'(t+1) = \mathbf{B}^* \mathcal{F}(\bar{\mathbf{x}} + \mathbf{B}\mathbf{x}'(t) + \mathbf{U}\mathbf{c}(t), \mathbf{w}(t)) - \mathbf{B}^* \bar{\mathbf{x}} \quad (11)$$

$$\mathbf{y}(t) = \mathcal{E}(\bar{\mathbf{x}} + \mathbf{B}\mathbf{x}'(t) + \mathbf{U}\mathbf{c}(t)) + \mathbf{n} \quad (12)$$

We now make an approximation to Eqs (11, 12), by assuming that the null space, $\mathbf{c}(t)$, is dynamically uncoupled from the reduced-state, $\mathbf{x}'(t)$, and can be treated as a statistically independent noise. That is, we approximate Eqs (11, 12), respectively, by,

$$\mathbf{x}'(t+1) = \mathbf{B}^* \mathcal{F}(\bar{\mathbf{x}} + \mathbf{B}\mathbf{x}'(t), \mathbf{w}(t)) + \mathbf{q} - \mathbf{B}^* \bar{\mathbf{x}} \quad (13)$$

$$\mathbf{y}(t) = \mathcal{E}(\bar{\mathbf{x}} + \mathbf{B}\mathbf{x}'(t)) + \mathbf{n}' + \mathbf{n} \quad (14)$$

The equations are now closed entirely within the coarse state. The new terms, \mathbf{q} and \mathbf{n}' , represent the formal errors due to the effects of the reduced model's unresolved physics (the null space, $\mathbf{c}(t)$.) For simplicity, we will make the assumption that \mathbf{q} and \mathbf{n}' are independent. On the other hand, the dynamic uncoupling assumption means that energy in the null space will largely remain in the null space, and therefore,

$$\mathbf{B}^* \mathcal{F}(\mathbf{U}) \approx \mathbf{B}^* \mathbf{U} = \mathbf{O} \quad (15)$$

so that \mathbf{q} can be expected to be small. In such case, the correlation between \mathbf{q} and \mathbf{n}' is secondary.

Note that a similar approximation is implicitly performed when writing Eqs (9, 10) to begin with. Since the underlying oceanic phenomena is continuous, any numerical model truncates the resolvable spectra similar to the approximation in Eq (3). The null space is the unresolvable scales and its effects are typically treated as being diffusive (e.g., eddy diffusion).

Equation (13) describes an approximation of the model with a reduced dimension. Alternatively, one may construct a reduced dimensional model by using a subset of the

original fine scale grid with the same model algorithm. However, model parameters such as mixing are usually dictated by model grid spacing (assuming the same finite differencing scheme), so that the resulting coarse grid model will have different physics than the fine scale model (Miller, 1986). Eq (13) avoids such discrepancies by using the same model parameters (\mathcal{F}) allowed by the higher order numerical scheme implicit in the transformed model, viz., the combination of the three operators, B^* , \mathcal{F} , and B . Alternatively, Eq (13) can be viewed as a spectral model based on the expansion defined by Eq (3).

All statistical quantities of the reduced-order model may now be estimated based on Eqs (13, 14), using standard Kalman filter equations (Riccati equation), and statistical properties of the original model will be approximated according to Eq (4) and in turn substituted into Eqs (1, 2) for assimilation. Such state dimension reduction greatly reduces the computational requirements of Kalman filtering, because the storage and matrix operations involved in Kalman filtering are proportional to the square and cube of the model dimension, respectively.

Alternatively, we may further simplify the filtering operations by approximating the time evolving model error, $\mathbf{P}'(\mathbf{t})$, by its asymptotic steady-state limit as described in the previous section, thereby further eliminating the continuous time-integration of matrix $\mathbf{P}'(\mathbf{t})$ as well. Such an error limit is computed based on a time-invariant approximation of the model dynamics (Eqs 13, 14). Non-stationary observations, in which the observation pattern or what variables are measured vary in time, can also be approximated as a stationary observation matrix for the purpose of deriving an approximate error (e.g., Fu et al., 1993; also see section 3.4 below.) For linear models ($\mathcal{F}(\mathbf{x}, \mathbf{w}) \equiv \mathbf{A}\mathbf{x} + \mathbf{G}\mathbf{w}$) and observations ($\mathcal{E}(\mathbf{x}) \equiv \mathbf{H}\mathbf{x}$), Eqs (13, 14) are written as,

$$\mathbf{x}'(t + 1) = \mathbf{A}'\mathbf{x}'(t) + \mathbf{B}^*(\mathbf{A} - \mathbf{I})\bar{\mathbf{x}} + \mathbf{G}'\mathbf{w} + \mathbf{q} \quad (16)$$

$$\mathbf{y}(t) = \mathbf{H}'\mathbf{x}'(t) + \mathbf{H}\bar{\mathbf{x}} + \mathbf{n}' + \mathbf{n} \quad (17)$$

where $\mathbf{A}' \equiv \mathbf{B}^*\mathbf{A}\mathbf{B}$, $\mathbf{G}' \equiv \mathbf{B}^*\mathbf{G}$, and $\mathbf{H}' \equiv \mathbf{H}\mathbf{B}$, and are linear time-invariant operators. The static limit of the assimilated model state covariance matrix is a function of these coefficient matrices (except terms involving the nonstochastic variable, $\bar{\mathbf{x}}$) and the error statistics of Eqs (16, 17), and can be computed efficiently by the “doubling algorithm” (Anderson and Moore, 1979). The doubling algorithm is a recursive matrix equation that integrates the state error covariance matrix in increasing time-steps of powers of

two, thus allowing convergence much faster than the Riccati equation (e.g., Fukumori et al., 1993).

We are unaware of theorems regarding the existence of asymptotic error limits for nonlinear models, as in the case for linear systems. However, it is plausible that there exists some error limit for nonlinear systems, even not in a steady-state, around which the true state error varies and which might be used as a reasonable approximation. For example, we definitely know the state of the ocean within certain bounds for either linear or nonlinear models. An optimistic approximation will be recognized by an excessive innovation series (difference between observation and model prediction) compared with the expected errors, and a pessimistic approximation will merely result in a slower convergence to the optimal estimate. Thus, we will seek an asymptotic error even for nonlinear systems. The simplest approach would be to linearize the model 3 and 4 around some fixed state, instead of the time-varying piecewise linearization of the extended Kalman filter (Gelb, 1974), and approximate the dynamic system into a linear system as in Eqs (16, 17) for the sole purpose of computing an approximate error. Consequently, results from linear theory are readily applicable to this approximate system.

It is emphasized that usage of asymptotic static errors are only meant to be *approximations*, and do not imply that the optimal estimation errors actually converge to these limits. Approximations are useful in as much as they provide improvements in the estimates, even though these improvements may only be partial just because they are approximations.

Matrices \mathbf{A}' , \mathbf{G}' , and \mathbf{H}' of Eqs (16, 17) can be constructed numerically (Fukumori et al., 1993). For instance, each column of \mathbf{A}' is obtained by integrating the corresponding column of the identity matrix by the model operator in Eq (13). An example for a general nonlinear model is described below; linearizing \mathcal{F} in Eq (13) about the reference state, $\bar{\mathbf{x}}$,

$$\begin{aligned}\mathbf{x}'(t+1) &= \mathbf{B}^* \mathcal{F}(\bar{\mathbf{x}} + \mathbf{B}\mathbf{x}'(t), \mathbf{w}) + \mathbf{q} - \mathbf{B}^* \bar{\mathbf{x}} \\ &\approx \mathbf{B}^* \mathcal{F}(\bar{\mathbf{x}}, \mathbf{w}) + \mathbf{B}^* \frac{\partial \mathcal{F}}{\partial \mathbf{x}} \bigg|_{\bar{\mathbf{x}}} \mathbf{B}\mathbf{x}'(t) + \mathbf{q} - \mathbf{B}^* \bar{\mathbf{x}}\end{aligned}\quad (18)$$

$$\approx \mathbf{A}' \mathbf{x}'(t) + \text{rest} \quad (19)$$

Then, the i 'th column of \mathbf{A}' , \mathbf{a}'_i , can be obtained by,

$$\mathbf{a}'_i \equiv \mathbf{A}' \mathbf{e}_i = \mathbf{B}^* \frac{\partial \mathcal{F}}{\partial \mathbf{x}} \bigg|_{\bar{\mathbf{x}}} \mathbf{B} \mathbf{e}_i \approx \mathbf{B}^* \mathcal{F}(\bar{\mathbf{x}} + \mathbf{B} \mathbf{e}_i, \mathbf{w}) - \mathbf{B}^* \mathcal{F}(\bar{\mathbf{x}}, \mathbf{w}) \quad (20)$$

where \mathbf{e}_i is the i 'th column of the identity matrix in the coarse domain, and the two terms on the right hand side are numerically evaluated using the model. Such numerical treatment of model dynamics makes utilization of complex numerical models straightforward for data assimilation. Note that \mathbf{A}' (as well as \mathcal{F} in Eq 9) denotes the state transition matrix over the observation time interval and not the individual model time step.

Once the static limit of the coarse resolution prediction error covariance matrix ($\mathbf{P}'(-)$) is obtained, it is substituted into Eq (2) using Eq (4) to get,

$$\begin{aligned}\mathbf{K}(t) &\approx \mathbf{B}\mathbf{P}'(-)\mathbf{B}^T\mathbf{H}^T(t)[\mathbf{H}(t)\mathbf{B}\mathbf{P}'(-)\mathbf{B}^T\mathbf{H}^T(t) + \mathbf{R}(t)]^{-1} \\ &\approx \mathbf{B}\mathbf{P}'(-)\mathbf{H}'^T(t)[\mathbf{H}'(t)\mathbf{P}'(-)\mathbf{H}'^T(t) + \mathbf{R}(t)]^{-1}\end{aligned}\quad (21)$$

The Kalman gain may also be approximated based on its alternate equivalent form written in terms of the data-updated covariance (e.g., Gelb, 1974);

$$\mathbf{K}(t) = \mathbf{P}(t)\mathbf{H}^T(t)\mathbf{R}^{-1}(t) \quad (22)$$

$$\approx \mathbf{B}\mathbf{P}'\mathbf{B}^T\mathbf{H}^T(t)\mathbf{R}^{-1}(t)$$

$$\approx \mathbf{B}\mathbf{P}'\mathbf{H}'^T(t)\mathbf{R}^{-1}(t) \quad (23)$$

$\mathbf{P}(t)$ is the error covariance matrix of the data updated estimate (eq 1), and \mathbf{P}' is the corresponding asymptotic limit of the coarse state. All matrices except \mathbf{B} and $\mathbf{P}'(-)$ (or \mathbf{P}') are time varying in general. Eqs (21) or (23) provide an approximate Kalman filter that can be applied to the original model with the full resolution;

$$\mathbf{x}(t) = \mathbf{x}(t, -) + \mathbf{K}_{approx}[\mathbf{y}(t) - \mathcal{E}(\mathbf{x}(t, -))] \quad (24)$$

where \mathbf{K}_{approx} is given by either Eqs (21) or (23), (The latter approximation, Eq (23), is easier to implement when \mathbf{H} or \mathbf{R} vary in time, as it will only involve matrix times vector operations besides the inverse of \mathbf{R} .) The filtered estimate, $\mathbf{x}(t)$, is then time-stepped by the original model (Eq 9), until a new set of observations are available, and once again assimilated according to Eq (2.4). We stress again that the linearized reduced dimensional model (Eqs 16, 17) is only used in obtaining the approximate error estimate for use in Eqs (21) or (23), and does not otherwise participate in the actual assimilation itself. Also note that the left most matrix of \mathbf{K}_{approx} (Eqs 21, 23) is \mathbf{B} . Therefore, the components of the model that will be directly modified by the data (Eq

24) is limited to the range space of B . For example, if B is an interpolation operator that transforms the large spatial scales onto the fine grid, the short scales present in the model prediction, $\mathbf{x}(t, -)$, are unmodified by Eq (24). However, smaller scales will subsequently be generated and modified by the model itself (\mathcal{F}) in the prediction phase of Kalman filtering; i.e., in computing $\mathbf{x}(t + 1, -)$ from $\mathbf{x}(t)$ by the original full resolution nonlinear model, Eq (9).

3. Assimilation Experiments

We now examine the utility of the approximations described in the preceding sections, in an identical twin experiment. A twin experiment is a simulation of data assimilation. Two model simulations are run starting from two independent initial conditions, from one simulation pseudo observations are taken and assimilated into the other, to see how well the state of the former can be estimated. The degree of how much the former state is recovered provides a measure of the observation's information content and the skill of the assimilation scheme.

The twin experiment examined in this study is the idealized Gulf Stream model of RY92 (Malanotte-Rizzoli and Young, 1992), whose motivation was provided by the SYNoptic Ocean Prediction (SYNOP) experiment carried out in the period 1987-1990 in the Gulf Stream system. The scientific objective of SYNOP was to understand the structure and variability of the system and to predict the evolution of the Stream density front. SYNOP consisted of three major arrays of moorings, the Inlet array, located at Cape Hatteras, where the Stream leaves the coast and meanders into the ocean interior; the Central array, located at $\sim 68^\circ\text{W}$, west of the New England Seamounts; and the Eastern array, located at $\sim 55^\circ\text{W}$. Figure 1 shows the actual field work configuration of SYNOP. The focus of RY92 was to examine whether constraints provided by localized arrays are strong enough for the model dynamics to reconstruct Gulf Stream processes, and was considered in an idealized model of the SYNOP experiment.

In the study of RY92, the Central and Eastern arrays were schematized as two identical arrays of moorings in an idealized zonal channel with an unstable east-west jet (Fig 2). The model is based on the Semispectral Primitive Equation Model (SPEM; Haidvogel et al., 1991), with a fixed inflow at the western boundary. The eastern end has a dynamic open boundary condition (Orlanski, 1976), whereas the northern and southern boundary conditions are free-slip, no-normal flow. The model uses the

rigid-lid approximation, and has advective nonlinearities in momentum and density. The model domain is 1875 km zonally, and 1400 km meridionally with a flat bottom at a constant depth of 4000 m. The total model grid is 129 x 97 horizontally with 5 collocation points in the vertical. The horizontal resolution is approximately 14 km, and a 20 minute model time stepping is used.

A control experiment is carried out by running a simulation for 300 days starting from an analytically prescribed form of a geostrophically and hydrostatically balanced, zonally uniform jet. The model is unstable, with meanders growing into large amplitudes, and pinching off eddies. The twin experiment is carried out as described in Fig 3. Pseudo measurements are taken at two day intervals between days 60 to 120 of the simulation, and are assimilated into the model, initialized to day 180 of the control run. For convenience, the first simulation from which pseudo data are obtained is referred to as the “true ocean” (days 60 to 120 of the control run), while the second simulation is the “false ocean” (days 180 to 240 of the control run). The assimilated estimate is the “model ocean” (initialized by day 180 of the control, but modified by the assimilation). The decorrelation time of the control run was approximately 12 days, and therefore the 60-day time separation between the “true ocean” and the “false ocean” can be regarded as statistically uncorrelated. Figure 4 shows an example of the evolution of the surface density anomaly in the “true ocean” (left panels) and the “false ocean” (right panels).

The assimilated measurements of RY92 included, current velocities, densities (temperatures), and transport stream functions (volume transports) at the two arrays of thirteen moorings (Fig 2) with measurements taken on each of the five depths at each location. Using a simple time-continuous nudging scheme, with the two-day pseudo data linearly interpolated in time, RY92 found that velocity measurements were effective in recovering the “true ocean”, where an event of meander formation, steepening, bending, and breaking off was resolved (denoted A through E in Fig 4). The meander event was localized in the region roughly between the two arrays, almost void of measurements. However, there was little improvement with density assimilation, and nudging stream function resulted in making the errors increase over the “false ocean.”

The simple “nudging” scheme used in RY92 involves appending to the model prognostic equations a forcing term that relaxes the model variables to the observations. The nudging factor, an inverse time scale, is a measurement of the weight given to the data versus the model predicted variables. Even though the nudging scheme proved

to be very successful, it is still a very crude assimilation. method. The information constrains the model only locally near the actual data points. It is left to the model dynamics to perform the advection of information from the data-dense to the data-void regions and from one measured prognostic variable to the unmeasured variables.

We will now revisit the questions raised by RY92 using the approximate Kalman filter, which is capable of spreading the localized information throughout the model domain and different variables in an optimal fashion. Additionally, assimilation of other types of observations will also be examined as to how well they constrain the estimation, including sea level from satellite altimetry and integrated measurements of acoustic tomography.

Sections 3.1 and 3.2 describe details of deriving the approximate filter presented in section 2 for this particular experiment, and readers interested in the results of the calculation may directly proceed to section 3.3 at first reading, without loss of continuity.

3.1 Coarse State Approximation and Linearization

The premise of the reduced state dimension approximation is two-fold; i) that the coarse state approximates the model's true state (Eq 3), ii) that the null space of the transformation, B , is approximately uncoupled from the range space dynamically (Eq 13). The selection of B will be described with regard to these requirements. The SPEM model is a primitive equation model, with the hydrostatic and rigid lid approximations, and the state vector consists of the two components of horizontal velocity and density on the three-dimensional grid. All other variables, such as vertical velocity and sea surface pressure, are computed diagnostically from these prognostic variables. The values along the open boundary are dynamically updated, and as such are also part of the state vector. The total state dimension without the coarse approximation is 172,252. As the model will later be linearized around the time-mean structure, the coarse state will be defined as variability around this mean ($\bar{\mathbf{x}}$), which is shown in Fig 5.

Based on requirement ii) above, the natural reduction in the vertical would be an expansion into linear dynamic modes, with their amplitudes constituting the elements of the state vector. Vertical expansion into dynamical modes show that the barotropic and first baroclinic modes together account for 99% of the total velocity variability and 76% for density. The lesser skill in density is due to the nonlinear nature of the model

jet; the baroclinic modes of density have zero amplitude at the surface and bottom, but the model's density variations are due to the strong advective nonlinearities, which require higher modes to resolve. However, inclusion of higher order density modes will necessitate the corresponding velocity modes to be included as well, and so were not made part of the approximation. On the other hand, the two horizontal components of the barotropic velocity are dependent due to the rigid-lid approximation and satisfy non-divergence. Therefore stream function or barotropic vorticity can replace velocity's two barotropic components, further reducing the state dimension. The present study will utilize the latter in the coarse state approximation.

There are no readily available dynamic modes in the horizontal dimension for the present study, so an alternative approach is taken. The spatial scale and structure of the dominant variability can be assessed by examining the structures of the empirical orthogonal functions (EOFs). Let \mathbf{Z} denote a matrix whose columns are the leading n EOFs of a vector, \mathbf{z} . Then, \mathbf{z} may be approximated as,

$$\mathbf{z} \approx \mathbf{Z}\mathbf{b} \quad (25)$$

where \mathbf{b} is a vector consisting of the EOFs' expansion coefficients, and is given by,

$$\mathbf{b} = \mathbf{Z}^T \mathbf{z} \quad (26)$$

Then,

$$\mathbf{z} \approx \mathbf{Z}\mathbf{Z}^T \mathbf{z} \quad (27)$$

and the matrix $\mathbf{Z}\mathbf{Z}^T$ is the resolution matrix, as in linear inverse theory, which describes the linear combinations of the elements of \mathbf{z} that are resolved by the n EOFs. Alternatively, the rows of $\mathbf{Z}\mathbf{Z}^T$ characterize the correlation among the elements of \mathbf{z} that dominate \mathbf{z} 's variability.

Fig 6 shows results of an EOF analysis of the meridional variations of the two velocity components and density, around the time-mean structure of the jet. It is found that from among the 96 degrees of freedom (95 for meridional velocity), 13 modes will account for at least 97% of the variability y for all three variables. The resolution matrix constructed by these thirteen modes is shown in Fig 7 for zonal velocity. The matrix is diagonally dominant, with its width narrowest about the axis of the jet and increasing towards the north and south boundaries. Based on this analysis, a coarse

meridional grid was chosen strategically as shown in Fig 8, with grid separation being approximately equal to the e-folding scale of the spatial correlation. A similar analysis was carried out for the zonal structure, and a set of 20 zonal grid points were chosen as also shown in Fig 8.

A bicubic interpolation scheme (B) is used to interpolate state values from the coarse horizontal grid onto the original fine resolution grid points. A sufficiently smooth interpolation scheme is required from condition ii) above. For example, a bilinear interpolation results in discontinuities in spatial gradients at the coarse grid boundaries, such that high wave number variabilities are generated when the model is integrated forward in time, which are no longer resolvable by the coarse grid. Alternatively, the EOFs themselves may be used to expand the state variabilities when they are sufficiently smooth. However, this choice was not made for the present study, because EOFs may artificially bias the twin experiment's results by explicitly building in the preferred structure of the "true" variability into the assimilation scheme.

The coarse approximations for the other state variables are similarly defined, which are slightly different from one another because of the staggered grid in the SPEM model ('C'-grid) and their respective boundary conditions. The total coarse dimension is 1399; 273 (21 zonal x 13 meridional) grid points for barotropic vorticity, 280 (20 x 14) and 260 (20x 13) for first baroclinic zonal and meridional velocities, respectively, 280 (20x 14) for barotropic and first baroclinic density, 13 each along the open boundary for barotropic meridional velocity and the meridional *gradient* of barotropic zonal velocity.

A test of the dynamic decoupling between the coarse state above and its null space is shown in figures 9 and 10. A comparison is made to examine whether a perturbation in the coarse state remains in the approximation's range domain over time. That is, the comparison is between $\mathcal{F}(\bar{\mathbf{x}} + \delta\mathbf{x}) - \mathcal{F}(\bar{\mathbf{x}})$ and $\mathbf{B}\mathbf{B}^*(\mathcal{F}(\bar{\mathbf{x}} + \delta\mathbf{x}) - \mathcal{F}(\bar{\mathbf{x}}))$, where $\delta\mathbf{x}$ is within the range space of the approximation, and 3 denotes a model integration over 2-days which is the time interval (observation period) of the approximation (Eq 13). Figs 9 and 10 are for a perturbation of the first baroclinic component of zonal velocity at one of the coarse grid points along the jet's axis; i.e., $\delta\mathbf{x} = \mathbf{B}\mathbf{e}$, where elements of \mathbf{e} are all zero except for the corresponding zonal velocity grid point. The figures show that the variability after two days are both approximately the same, in the vertical and the horizontal, between the full resolution and its coarse approximation.

An example of the model's actual state and its coarse representation is shown in Fig 11, in which the model's transport stream function at day 88 (1 la) is compared with its coarse approximation (1 lb). The two are virtually identical to the eye. Fig 12 shows a comparison of the temporal change in the model (12a) between days 88 and 90 with that estimated by the coarse approximation (12b-d). The temporal change in the coarse state (12b) resolves most of the structures in the model's evolution (12a), and the coarse model (12c) accounts for the dominant structure in 12b, further demonstrating the dynamic decoupling between the coarse representation and its null space.

The linearized state transition matrix was numerically computed as described by Eq (20), around the time-mean structure of the jet (Fig 5). In practice, since the model variables are dimensional, a scaling factor is multiplied to e_i and the result, \mathbf{a}'_i , later rescaled by the same to avoid numerical inaccuracies. The scaling factor was chosen to be 1% of the temporal variability of the jet's coarse approximation.

Fig 12d shows the temporal change of the jet based on this linearized state transition matrix. The figure shows the gross structure of the jet's evolution being resolved, as compared with the fully nonlinear evolution shown in Fig 12c. However, the amplitudes of the time-change are somewhat larger than those of the nonlinear evolution, and are due to linear instability. Fig 13 shows the magnitudes of the linearized state transition matrix' eigenvalues. All eigenvalues are distinct, among which 48 have moduli larger than or equal to one corresponding to unstable and neutral modes, respectively. These modes reflect the linear instability of the jet, and would grow indefinitely in the linear model because of the absence of nonlinear equilibration that is otherwise present in the unapproximated model. Lack of such equilibration must properly be taken into consideration when integrating the errors with the linearized model, and this issue will be addressed in the following section. Nevertheless, the similarities among the comparisons show that the present choice of the coarse approximation and linearization, resolve some of the gross nature of the jet's dynamics, and therefore, the error estimates computed under these assumptions can be expected to at least approximate some aspects of the true error evolution.

3.2 Computation of the Approximate Kalman Filter

The observation matrix in the coarse space, \mathbf{H}' , may be computed numerically as in the computation of the linearized state transition matrix (Eq 20). Namely each column of \mathbf{H}' is computed by mapping a column of the identity matrix in the coarse

domain into the fine resolution, from which the observed quantity is computed as in the forward model computation. The observation matrix is rather trivial when the measurement is one of the state elements, but becomes complex when the observation is a nontrivial function of the state, such as the stream function, or altimetric and tomographic measurements discussed later in sections 3.3 and 3.4. Many algorithmic simplifications are achieved by this numerical formulation, as is also the case with the state transition matrix (section 2.2).

In order to formulate the Kalman filter, one further needs an estimate of the observation error and the model's process noise covariance matrices, besides the transition matrix and the observation matrix. Strictly speaking, being an identical twin experiment, the present simulation is pathological, having zero process noise and observation error (no artificial error is added to the pseudo measurements), and the only error source is the errors associated with the initial condition. Thus, if the model is fully observable and ignoring model nonlinearities, the estimation errors will eventually become zero, and the “true ocean” will be fully recovered by the “model ocean”.

However, the model dimension does not allow such a computation, which is why we resort to the present approximate filter. The approximate filter has sources of errors due to the unresolved small scale variability, which are present in the observations but whose interactions with the coarse state are not dynamically modeled (\mathbf{q} , \mathbf{n}' in Eqs 13, 14). Such errors are estimated below, which will be validated a posteriori from the results of the assimilation.

The observation error of the reduced dimension approximation is due to the variations associated with the small scales not resolved by the coarse state transformation (\mathbf{n}' in Eq 14). An estimate of such contributions can be made by comparing the simulation's variabilities and their coarse representations. Based on such analyses, the observation errors were treated as being white horizontally, with variance equaling the root-mean-square difference between the fine state (\mathbf{Hx}) and its coarse representation ($\mathbf{H}(\mathbf{B}\mathbf{B}^*(\mathbf{x}-\bar{\mathbf{x}})+\bar{\mathbf{x}})$). Vertically, the errors were modeled in terms of the SPEM model's Chebychev modal expansion, with each amplitude being uncorrelated with the others.

The Kalman filter assumes the observational errors ($\mathbf{n}' + \mathbf{n}$ in Eq 17) to be white in time. However, the small scale variations are correlated over the two-day observation period. For example, small eddies unresolved by the coarse approximation last much longer than two-days. In such circumstances, the model will become overconstrained

by the correlated errors unless the measurements are whitened. Gelb (1974) describes such whitening methods by differencing the measurements. In the present situation, a simpler approximation is made in which we increase the observational errors by some factor, β , and thereby effectively reducing the significance of the correlated measurements. Such simplifications are sensible, realizing that the present calculation is only aiming to derive an approximate model error. Several β values were experimented with (as well as for γ and α below), and the combination with the best skill with consistent estimation errors (e.g., Fig 22) are presented below. This error increase factor, β , was set to 10 for the results below.

The reduced-dimension approximation's process noise (q in Eq 13) is due to the interactions between the coarse state and the small scale variability unresolved by the approximation. This error source is difficult to evaluate, and as such we shall model it simply as being a white noise in the coarse domain, with variance proportional to the time-mean variance of the simulation's coarse state representation. The proportionality factor (γ) was set equal to 0.1. On the other hand, due to the difference in spin-up time-scale, this specification will lead to a relative overestimate of the baroclinic component over the barotropic part (e.g., Fukumori et al., 1993). Furthermore, an additional source of process noise exists for density, because the quasi-geostrophic modes do not adequately describe the density variations as discussed in section 3.1. Therefore, an additional factor was multiplied to γ for each separate coarse state variable. These factors, $(\gamma_\zeta, \gamma_u, \gamma_v, \gamma_{\rho 0}, \gamma_{\rho 1})$, for barotropic vorticity, the two components of first baroclinic velocity, and the barotropic and baroclinic density, respectively, were set to (2, 0.5, 0.5, 4, 2).

The asymptotic steady-state error is computed by the doubling algorithm (Anderson and Moore, 1979). Such limit can be shown to exist uniquely, if the unstable and neutral modes of the model are both observable and stochastically controllable (Goodwin and Sin, 1984). Observability is the ability to determine the state from observations in the absence of errors, and stochastic controllability is the ability to force the model from one arbitrary state to another by the model process noise (e.g., Gelb 1974). In particular, a mode can be shown to be observable when the norm of its projection with the observation matrix is nonzero (Hautus, 1969). Fig 13 demonstrates that the model is fully observable by the velocity observations, and since process noise was modeled as being white, all modes are also controllable. Therefore, the asymptotic error limit

exists for the present linearized model. (See, for example, Fukumori et al. (1993) for more details regarding the existence and computation of the asymptotic static filter.)

Although an asymptotic steady-state error exists, the computed limit turns out to be larger than the natural variability of the jet, and the approximate filter constructed from this limit did not resolve the “true ocean” satisfactorily. The failure of the assimilation is due to the unrealistic model error estimate that is larger than the jet’s variability, which results because of the model’s time-invariant linearization used for error integration. That is, although formally completely observable, error growth associated with the linear instability evolves into unrealistic error amplitudes until balanced by the observations, whereas, in reality, error growth will further be equilibrated by nonlinear dynamics (e.g., Fig 12).

To account for the deficiencies of the time-invariant linearization, we assumed contributions from artificial observations of the entire state in the model error integration, in order to simulate the effects of nonlinear equilibration which is present in the unapproximated model used to integrate the model state itself. The error covariance of these artificial observations were treated as being white, and its variance comparable to the natural variability of the jet. For, after all, even without assimilation, the “model ocean” remains within natural variability from the “true ocean”. This error variance was assumed to be ten times (α) larger than the variance of the simulation. It should be emphasized that these observations are artificial, in that their effects are assumed only during state error estimation for the approximate filter. That is, extra rows corresponding to these ‘artificial observations’ are added to H' during the doubling algorithm to compute error limits $P'(-)$ and P' , but are not included in H' of the filter itself (Eqs 21 or 23).

3.3 Assimilation of Localized Clusters Revisited

We now revisit some of the assimilation experiments carried out by RY92, using the approximate Kalman filter described in the preceding sections. Three assimilation experiments are examined in this section;

- (1) Velocity data only
- (2) Total transport data only (stream function)
- (3) Density data only

The results of the density assimilation discussed below is based on a larger observation error (proportionality factor, β) than what was presented in section 3.2 and used

for the other experiments. The observation error estimate computed in section 3.2, is an underestimate for density, since density variations are largely due to advection, which the linearized model does not properly simulate. Therefore, β was set to 100, to take this additional missing physics into account.

The resulting sea surface density for these assimilations are shown in figures 14, 15, and 16, which are to be compared with Fig 4. The velocity assimilation resolves the major meander of the “true ocean” (labeled A and B in Fig 4), while at the same time suppresses the southward meander of the “false ocean” (F in Fig 4). On the other hand, the density assimilation, although resolving some of the variability (e.g., the northern and southern, westward propagating anomalies labeled D and E in Fig 4), is unsuccessful in estimating the meanders and there’ appears to be a significant amount of error. Although these findings are qualitatively consistent with the results of RY92, Fig 15 shows that the estimates made by assimilating transport stream functions are as good as the velocity assimilation, contrary to RY92’s result, *in* which stream function assimilation was found ineffective, and which even degraded the estimates compared to the “false ocean” (see fig 19 described below). The present results suggest that, contrary to previous analyses, the information content of transport measurements can be as good as an array of individual velocity observations, and that RY92’s nudging scheme used for stream function is less optimal than their scheme for velocity assimilation.

Similar to RY92, a quantitative measure of the assimilation’s accuracy is given by the root-mean-square (rms) difference between the assimilated estimate and the “true ocean” at a particular depth,

$$\sigma_{\text{assimilation}} = \sqrt{\frac{\sum_N (f_{\text{assimilation}} - f_{\text{true}})^2}{N}} \quad (28)$$

where N is the total number of grid points and f denotes one of the state variables. These rms errors will be analyzed relative to the corresponding rms errors of the false ocean, shown in figure 17. Also shown in fig 17 are the errors of RY92. The difference between the present simulation and RY92 is due to the slightly different versions of the SPEM model used in the two studies. The present version is more unstable, and results in a larger error in the false ocean than in RY92. This can also be seen by comparing the model simulations shown in Fig 4 with the same in RY92 (their Fig 8), in which the present model has stronger short scale variabilities than RY92.

Figures 18, 19 and 20 show therm's errors for the three experiments relative to those of the "false ocean"; $e_{\text{assimilation}}/e_{\text{false}}$. Relative errors smaller than unity indicate improved estimates by the assimilation over the "false ocean". The errors in fig 18 gradually decrease relative to the "false ocean" as information from the observations accumulate, whereas fig 19 shows an immediate improvement reflecting the fast spin-up time-scale of the barotropic mode. In all cases, the errors of the present approximate Kalman filter are much smaller than those in RY92 (except for density towards the end, discussed later), demonstrating the filter's superior skill. Many of the assimilation's errors also show some immediate (day 60) improvement over the "false ocean" even for variables that are not directly assimilated, such as density for both the velocity and stream function assimilations, which reflects the nontrivial correlation established by the model. The errors become smaller for velocity assimilation (Fig 18) than for stream function (Fig 19), but that alone does not indicate a generic lack of information content of the latter compared with the former. The primary difference is in the amount of measurements; there are 260 measurements of velocity components per 2-day period in the twin experiment, whereas there are only 26 stream function measurements.

The density assimilation (Fig 20) shows a smaller improvement over the "false ocean" compared with velocity and stream function assimilation, and even results in an excess error towards the end. The relative ineffectiveness of density assimilation in estimating the "true" state is due to the nature of the jet's variability. Fig 21 shows the meridional gradient of absolute vorticity for the reference time-mean state of the jet ($\bar{\chi}$). There is a sign change across the jet's axis, indicating the necessary condition for barotropic instability being satisfied. In fact, a detailed examination of the energetic of the jet around the major meander (A in Fig 4) shows that conversion of mean velocity shear is the largest energy source of eddy kinetic energy, and is larger than the conversion of available potential energy by a factor of eight. Density observations only provide information about available potential energy, and therefore is not sufficient to resolve barotropic instability, which is the dominant variability of the model jet.

Density is strongly affected by advection, and the excess errors at the end of Fig 20 appear to be due to the time-invariant linearization used in deriving the approximate filter; accumulated errors result in a barotropic instability not present in the "true ocean". A possible remedy would be to remove or periodically update the static assumption part of the filter approximation for such strongly nonlinear properties. RY92's

density assimilation has larger errors than the results of the approximate **Kalman** filter as in other cases, except towards the end, which is likely due to the more stable model used in RY92 (cf. Figure 17), rather than due to the differences in assimilation scheme per se.

Finally, the consistency of the assimilation is examined by comparing the differences between the true state and the estimate, with the expected uncertainties of the assimilation. Fig 22 shows the normalized error for the velocity assimilation experiment. All errors are on the order of one demonstrating the first order consistency of the approximate **Kalman** filter, which in turn indicates that the assumptions made for the observation errors and process noise (section 3.2) are sensible and not grossly unrealistic.

3.4 Assimilation of **Altimetric** and Tomographic Data

We next explore the problem of assimilating other non-traditional forms of observations. Measurements made by satellite altimetry and acoustic tomography are examined. The purpose of this section is not so much as to assess the information content of these observing systems, but to explore the utility of the approximate filter in assimilating these types of observations.

These two measuring systems are currently receiving much attention with respect to data assimilation, primarily because of their enormous data collection rate compared with other forms of measurements. A single satellite covers the globe several times a day with an along track measurement spacing of less than 10 km, and ray paths of acoustic tomography arrays increase geometrically with the number of source/receiver pairs. Another aspect of these observing systems is their complex sampling characteristics. Satellites sample the ocean surface according to orbit dynamics, laying down convoluted ground tracks (cf. Wunsch, 1989), and tomography measures integrated properties along curved ray paths. Data assimilation provides an effective framework to deconvolute these measurements, by effectively interpolating and extrapolating the measurements dynamically through space and time.

These two observing systems also differ from the situations of the previous section, in that they do not provide direct measurements of the models' prognostic variables. Several authors have examined assimilation by either assuming a correlation between the measurement and some of the model variables, such as correlating temperature profiles with sea level, or to invert and map the measurements into model variables

first, such as performing tomographic inversions prior to assimilation. This relationship between measurement and model variables is only a superficial difference, and estimation theory does not distinguish between them. All that is required to perform estimation is the forward theoretical relationship between the model's state variables and what is observed, Eq (10), and the Kalman filter readily treats these nontraditional measurements on the same footing as direct measurements of the model state elements themselves without intermediate inversions.

Pseudo altimetric measurements were made along a set of tracks shown in Fig 23. To simulate the repeat period of the satellite measurement and the existence of its subcycles, the sea' level observation points are alternated between the crosses and the diamonds every 2-days. Although the SPEM model uses the rigid lid approximation, pressure gradients along the surface can be diagnostically computed from the model state and inverted for pressure. Sea level is in turn related to pressure by the hydrostatic relation. Because of the model's advective nonlinearities, this functional relationship between state variables and sea level is nonlinear. The observation operator, H' , was, therefore, obtained by linearizing this relationship about the time-mean jet ($\bar{\mathbf{x}}$), as in the derivation of the linearized state transition matrix (Section 2.2). Sea levels are assimilated on alternating tracks (crosses and diamonds), and therefore the observation matrix, H , is not time-invariant (section 2.1). Nevertheless, as an additional approximation, an asymptotic error was computed assuming that the observations are present on both tracks simultaneously (but not during the actual filtering.) The resulting sea surface density evolution of the sea level assimilation is shown in Fig 24. As in previous experiments, the meanders are resolved by the assimilation, and the actual errors are greatly reduced from the "false ocean" (Fig 25). As a result of the added spatial coverage compared with the pseudo mooring assimilations in the previous section, the eddy (H in Fig 4) in the eastern domain is suppressed in Fig 24. However, the southward meander (C in Fig 4) is not resolved well, as it is not sampled by the altimetry tracks (Fig 23).

In light of the analysis of density assimilation in section 3.3, tomographic measurements of density (temperature) is not expected to be effective for the present simulation either, because of the dominance of barotropic instability. Therefore, instead, we shall examine pseudo reciprocal tomographic measurements in which mean velocity along

ray paths are assimilated. Fig 26 shows the array configuration for this pseudo reciprocal tomography, where there are 22 pairs of measurements. For simplicity, we shall assume the ray paths to be horizontal and that measurements are available only at mid-depth (2000 m), as opposed to actual multiple vertical ray paths between sources and receivers. Velocity projections onto the rays were integrated along each pair in Fig 26 and assimilated every 2-days. The resulting sea surface density (Fig 27) shows the meanders being resolved as in previous experiments. However, as the data are limited to averages over long distances, some small scale differences from the “true ocean” are more noticeable, in particular eddies 1% and E' in Fig 27. Reductions of the relative errors are shown in Fig 25. The smaller relative skill compared with other experiments is due to the difference in the assimilated amount of information. For example, any pair of stream function measurements provide similar information as do the pseudo reciprocal tomography, but the number of such pairs in the stream function experiment is 325, as opposed to 22 for the present experiment.

4. Summary and Discussion

An approximate Kalman filter was derived and successfully used for data assimilation with an ocean general circulation model. The model is an idealized Gulf Stream, and is based on a nonlinear primitive equation model with a large dimension of over 170,000 state elements. The model has an unstable jet with an open horizontal boundary and a rigid lid. The effectiveness of assimilating various types of pseudo observations was examined including localized measurements of velocity, density, and volume transport, and indirect measurements by pseudo satellite altimetry and acoustic tomography. These examples are some of the most complex ocean models that have been analyzed with estimation theory, in terms of the model's algorithm, size, dynamics, and types of measurements.

The approximate filter involves a state dimension reduction scheme based on a spatio-dynamic transformation, an asymptotic steady-state error covariance matrix, and a time-invariant linearized dynamic model for the Riccati equation. The filter was shown to successfully estimate the model state, except for the case of density assimilation, which proved relatively inefficient for the present simulation because of the jet's dominant barotropic instability and strong advective nonlinearities. The assimilated

results were found to be more accurate than what was estimated using a simpler nudging scheme, except for density assimilation at the end of the experiment, which appears to be “due to differences in the models employed. Despite the dramatic simplifications in deriving the approximate filter, the results demonstrate that the filter retains sufficient properties of the optimal solution to be useful.

The significance of the present study is several-fold. One, that a suboptimal Kalman filter based on an approximate model error estimate was demonstrated to generally outperform an empirical assimilation scheme (nudging). Two, that approximate model errors can be computed practically even for large complex general circulation models by the proposed method. Formulation by estimation theory readily puts complex observations such as altimetry and tomography on the same footing as other direct measurements of the state variables, which otherwise are difficult to assimilate by strictly empirical methods.

The computational requirements of the present calculation is minimal. The most time-consuming step turns out to be the numerical construction of the linearized coarse state transition matrix, Eq (20). To minimize the necessary computations, the two-day transition matrix was computed by first constructing an equivalent transition for six hours and then multiplying this matrix with itself. Derivation of the six hour transition matrix required 130 CPU minutes on a Cray Y/MP (2.6 Mw memory). (The matrix multiplication to convert to a 2-day transition required a mere 18 CPU seconds.) The computation of the asymptotic steady-state error is the largest computation besides the transition matrix, which, for the present coarse dimension of 1399, required 7 Mw of memory and 27 CPU minutes to perform 10 doubling iterations. (The doubling actually converged around the eighth iterate.) Given the approximate Kalman filter, the computational overhead of the actual filtering relative to a simulation is negligible, since filtering only involves matrix-vector operations; both required approximately 20 Cray Y/MP minutes to perform a 60-day integration. Many of the calculations deriving the approximate filter are well suited for the emerging massively parallel supercomputers and therefore can benefit greatly by their development. The computation of individual columns of the state transition matrix is independent among different columns and therefore are completely parallelizable. The doubling algorithm is a recursive matrix multiplication and inversion, for which parallel algorithms exist.

Virtually all practical assimilation schemes are approximations to the optimal estimate. However, the implicit statistical assumptions are rarely discussed, nor estimates of the final result's accuracies provided. The present approximate Kalman filter makes these assumptions explicit for examination, and provides an approximate measure of accuracy which is essential in evaluating the consistencies of the assumptions and testing the validity of the dynamic models (e.g., Fu et al., 1993).

The information content of various data types, or their effectiveness for estimation, can be measured by examining the reduction in the estimate's expected errors. However, optimal observing system design is beyond the scope of the present study and the results must properly be placed in context with regards to the model's physics and properties of the measurements, such as their amount and accuracies. For example, although density measurements were found ineffective in the present simulation, such would not likely be the case for a stable, oceanic condition, or if baroclinic instability were dominant. Error reduction also depends on the amount of assimilated data; for example, there were 260 pseudo velocity measurements as opposed to 26 for stream function. There are two aspects to data error. One is the actual measurement error, and the other is contributions from missing model physics. The former is obvious and was not part of the identical twin experiment, but becomes a central issue in comparing real observing systems. The latter, for the present simulation, is the small scale variabilities unresolved by the coarse approximation, and the strong advective effects of density. The effectiveness of data will be lessened if the effects of the unmodeled physics on the measurements are large.

Observability characterizes one aspect of the data's information content. However, as demonstrated, although observability pertains to whether the model state can be constrained by the measurement, it does not indicate how well it will do so. An analysis of the estimation errors, in particular, its reduction from the case without assimilation is critical.

To first order, the error estimates of the present simulation were found to be consistent with the actual errors. However, there are several indications that they are not accurate. For example, figure 22 shows that actual errors are still decreasing with time at the end of the experiment. Apparently, 60 days is too short for the estimation errors to truly converge. Additionally, the normalized errors (Fig 22) suggest that baroclinic velocity errors are overestimated whereas those for density are underestimated. We

have used the simplest model for the process noise, by assuming that they are uncorrelated among different state variables with ad hoc relative magnitudes. Although the present approximation was demonstrated to be useful in estimation, more accurate characterization of model process noise is needed.

The horizontal grid was made identical between the barotropic and first baroclinic modes. In retrospect, this is not an optimal choice, as baroclinic modes have smaller horizontal length scales. Added resolution for the baroclinic mode would have increased the computational cost due to the larger state dimension. However, if the small horizontal scales can be approximated to be independent of processes at a distance, the error covariances may be computed locally. For example, Parish and Cohn (1985) proposed a band-limited approximation and algorithm for evaluating the error covariance matrix. The possibility of combining the present reduced-dimension approximation and a localized computation of the error covariance warrant further examination. Although only filters have been explored in this study, the state reduction can easily be applied to approximate smoothers as well. These and other issues including use of more realistic process noise are left for future investigations.

Acknowledgements

Helpful discussions and suggestions to an earlier version of the manuscript by Lee-Lueng Fu and Victor Zlotnicki are gratefully acknowledged. Roberta Young helped set up the model for the simulations. This research was carried out in part by the Jet Propulsion Laboratory, California Institute of Technology, under contract with the National Aeronautics and Space Administration, PMR was supported by NASA through Grant #958208 (subcontract to MIT from JPL) and by the Office of Naval Research, Grant N00014-90-J-1481. Computations were performed on the Cray Y-MP of the Supercomputing Project at the Jet Propulsion Laboratory.

References

- Anderson, B. D. O., and J. B. Moore, 1979. "Optimal Filtering", Prentice-Hall, Inc., Englewood Cliffs, N. J., 357 pp.
- Bennett, A. F., and W. P. Budgell, 1987. Ocean data assimilation and the Kalman filter: Spatial regularity, *Journal of Physical Oceanography*, **17**, 1583-1601.
- Fu, L.-L., L. Fukumori and R. N. Miller, 1993. Fitting dynamic models to the Geosat sea level observations in the Tropical Pacific Ocean. Part II: A linear, wind-driven model, *Journal of Physical Oceanography*, **23**, 2162-2181.
- Fukumori, L., J. Benveniste, C. Wunsch and D. B. Haidvogel, 1993. Assimilation of sea surface topography into an ocean circulation model using a steady-state smoother, *Journal of Physical Oceanography*, **23**, 1831-1855.
- Gelb, A., 1974. "Applied Optimal Estimation", M.I.T. Press, Cambridge, MA 374 pp.
- Ghil, M., and P. Malanotte-Rizzoli, 1991. Data assimilation in meteorology and oceanography, *Advances in Geophysics*, B. Saltzman, cd., Academic Press, vol. 33, 141-266.
- Goodwin, G. C., and K. S. Sin, 1984. "Adaptive Filtering Prediction and Control", Prentice-Hall, Inc., Englewood Cliffs, N. J., 540 pp.
- Haidvogel, D. B., J. Wilkin and R. Young, 1991. A semi-spectral primitive equation ocean circulation model using vertical sigma and orthogonal curvilinear coordinates, *Journal of Computational Physics*, **94**, 151-185.
- Hautus, M. L. J., 1969. Controllability and observability conditions of linear autonomous systems, *Proceedings of the Koninklijke Nederlandse Akademie van Wetenschappen, Series A*, 443-448.
- Holland, W. R., and P. Malanotte-Rizzoli, 1989. Assimilation of altimeter data into an ocean circulation model: space versus time resolution studies, *Journal of Physical Oceanography*, **19**, 1507-1534.
- Kindle, J. C., 1986, Sampling strategies and model assimilation of altimetric data for ocean monitoring and prediction, *Journal of Geophysical Research*, **91**, 2418-2432.

- Malanotte-Rizzoli, P., and W. R. Holland, 1986. Data constraints applied to models of the ocean general circulation. Part I: the steady case, *Journal of Physical Oceanography*, 16, 1665-1682.
- Malanotte-Rizzoli, P., and W. R. Holland, 1988. Data constraints applied to models of the ocean general circulation. Part II: the transient case, *Journal of Physical Oceanography*, 18, 1093-1107.
- Malanotte-Rizzoli, P., R. E. Young, and D. B. Haidvogel, 1989. Initialization and data assimilation experiments with a primitive equation model, *Dynamics of Atmospheres and Oceans*, 13, 349-378.
- Malanotte-Rizzoli, P., and R. E. Young, 1992. How useful are localized clusters of traditional oceanographic measurements for data assimilation?, *Dynamics of Atmospheres and Oceans*, **17**, 23-61.
- Marotzke, J., and C. Wunsch, 1993. Finding the steady state of a *general* circulation model through data assimilation: application to the North Atlantic Ocean, *Journal of Geophysical Research*, 98, 20149-20167.
- Marshall, J. 1985. Determining the ocean circulation and improving the geoid from satellite altimetry, *Journal of Physical Oceanography*, **15**, 330-349.
- Martel, F., and C. Wunsch, 1993. The North Atlantic circulation in the early 1980s — An estimate from inversion of a finite difference model, *Journal of Physical Oceanography*, 23, 898-924.
- Mellor, G. L., and T. Ezer, 1991. A Gulf Stream model and an altimetry assimilation scheme, *Journal of Geophysical Research*, 96, 8779-8795.
- Miller, R. N., 1986. Toward the application of the Kalman filter to regional open ocean modelling, *Journal of Physics/ Oceanography*, 16, 72-86.
- Miller, R. N., and M. A. Cane, 1989. A Kalman filter analysis of sea level height in the tropical Pacific, *Journal of Physical Oceanography*, **19**, 773-790.
- Moore, A. M., and D. L. T. Anderson, 1989. The assimilation of XBT data into a layer model of the tropical Pacific Ocean, *Dynamics of Atmospheres and Oceans*, **13**, 441-464.

- Orlanski, I., 1976. A simple boundary condition for unbounded hyperbolic flows., *Journal of Computational Physics*, 21 , 251-269 .
- Parish, D. F., and S. E. Cohn, 1985. A Kalman filter for a two-dimensional shallow water model: formulation and preliminary experiments, *Office Note 904*, National Meteorological Center, Washington DC 20233, 64 pp.
- Robinson, A. R., 1992. Shipboard prediction with a regional forecast model, *Oceanography*, 1, 42-48,
- Robinson, A. R. and W. Leslie, 1985. Estimation and prediction of oceanic eddy fields, *Progress in Oceanography*, 14, 485-510.
- Robinson, A. R., M. A. Span, L. J. Walstad, and W. G. Leslie, 1989. Data assimilation and dynamical interpolation in Gulfcast experiments, *Dynamics of Atmospheres and Oceans*, 13, 301-316 .
- Semtner, A. J., and R. M. Chervin, 1992, Ocean general circulation from a global eddy-resolving model, *Journal of Geophysical Research*, 97 , 5493-5550 .
- Sheinbaum, J., 1989. Assimilation of oceanographic data in numerical models, Ph.D. thesis, University of Oxford, Oxford, England, 156 pp.
- Smedstad, D. M., and J. F. O'Brien, 1991. Variational assimilation and parameter estimation in an equatorial Pacific Ocean model, *Progress in Oceanography*, 26, 179-241.
- White, W. B., C.-K. Tai, and W. R. Holland, 1990a. Continuous assimilation of Geosat altimetric sea level observations into a numerical synoptic ocean model of the California Current, *Journal of Geophysical Research*, 95 , 3127--3148 .
- White, W. B., C.-K. Tai, and W. R. Holland, 1990b. Continuous assimilation of simulated Geosat altimetric sea level into an eddy-resolving numerical ocean model, 1. Sea level differences, *Journal of Geophysical Research*, 95 , 3219-3234 .
- White, W. B., C.-K. Tai, and W. R. Holland, 1990c. Continuous assimilation of simulated Geosat altimetric sea level into an eddy-resolving numerical ocean model, 2. Referenced sea level differences, *Journal of Geophysical Research*, 95 , 3235-3252 .
- Wunsch, C., 1989. Sampling characteristics of satellite orbits, *Journal of Atmospheric and Oceanic Technology*, 6, 891-907.

Figure Captions

Figure 1: Observational plan of the SYNOP Experiment. Solid blocks: location of current meter moorings. Solid triangles in the square comprising the southern part of the Eastern array: tomographic transceivers.

Figure 2: Configuration of the two clusters of pseudo moorings in the twin experiments used by Malanotte-Rizzoli and Young (1992) and the present study.

Figure 3: Schematic diagram describing the twin experiment. Pseudo measurements are taken at two day intervals and assimilated into a model with an independent initial condition.

Figure 4: Time evolution of surface density anomaly for the “true ocean” and the “false Ocean”. A meander (labeled A) emerges on day 82, growing to finite amplitude (B), which begins to break on day 106 (C), and disintegrating by day 118, leaving a warm (D) and cold (E) anomaly north and south of the jet that propagate westward. In contrast, the “false ocean” generates a southward meander (F), which eventually breaks, leaving a cold eddy (G) to the south. The false ocean also has a strong eddy (H) north of the jet, which gradually propagates to the west and towards the jet. Contour interval is 10^{-5} g/cm^3 .

Figure 5: Time-mean structure of the jet. The figures are, (a) transport stream function (c.i. = $2 \times 10^{13} \text{ cm}^3/\text{s}$) and (b) surface density anomaly (c.i. = 10^{-5} g/cm^3).

Figure 6: Percentage variance accounted for by meridional empirical orthogonal functions. The variance is the variability around the time-mean jet (Fig 5). u , v , and ρ denote zonal and meridional velocity and density, respectively.

Figure 7: The resolution matrix of the thirteen dominant meridional EOFs of zonal velocity. Contour interval is 0.5.

Figure 8: The coarse grid of zonal velocity, u . Solid lines indicate the coarse grid, whereas axis labels denote the fine grid. The coarse grid for u consists of 20 zonal (including the open boundary at the eastern end) and 14 meridional elements (including the north and south boundaries.)

Figure 9: Total variance of perturbation after 2-days as a function of Chebychev modal amplitudes. The perturbation ($\delta \mathbf{x}$) corresponds to a change in the first baroclinic

mode amplitude of zonal velocity at one of the coarse grid points along the jet's axis ($i, j = 67, 47$). The solid line corresponds to the full resolution model ($\mathcal{F}(\bar{\mathbf{x}} + 6\mathbf{x}) - \mathcal{F}(\bar{\mathbf{x}})$) and the dashed line is its coarse approximation ($\mathbf{B}\mathbf{B}^*(\mathcal{F}(\bar{\mathbf{x}} + 6\mathbf{x}) - \mathcal{F}(\bar{\mathbf{x}}))$).

Figure 10: Horizontal structure of the perturbation of Fig 9 after 2-days. The figure is for density's second Chebychev mode amplitude in the vicinity of the perturbation. The left panel (a) corresponds to the full resolution model, and the right panel (b) is its coarse approximation.

Figure 11: Transport stream function at day 88 of the simulation; (a) the full resolution model, \mathbf{x} , (b) the coarse approximation of (a), $\bar{\mathbf{x}} + \mathbf{B}\mathbf{B}^*(\mathbf{x} - \bar{\mathbf{x}})$. Contour interval is $2 \times 10^{13} \text{ cm}^3/\text{s}$.

Figure 12: Temporal change of stream function. from day 88 to day 90; (a) the full resolution model, $\mathbf{x}(90) - \mathbf{x}(88)$, (b) coarse approximation of (a), $\mathcal{C}(\mathcal{C}^*(\mathbf{x}(90))) - \mathcal{C}(\mathcal{C}^*(\mathbf{x}(88)))$, where $\mathcal{C}(\mathbf{x}') \equiv \mathbf{B}\mathbf{x}' + \bar{\mathbf{x}}$ and $\mathcal{C}^*(\mathbf{x}) \equiv \mathbf{B}^*(\mathbf{x} - \bar{\mathbf{x}})$ denote the coarse-to-fine and fine- to-coarse transformations, respectively, (c) the coarse model, $\mathcal{C}(\mathcal{C}^*(\mathcal{F}(\mathbf{x}_c(88), \mathbf{w}(88)))) - \mathbf{x}_c(88)$, where $\mathbf{x}_c \equiv \mathcal{C}(\mathcal{C}^*(\mathbf{x}))$ and is the coarse representation, (d) the linearized coarse model, $\mathcal{C}(\mathbf{A}'\mathcal{C}^*(\mathbf{x}(88)) + \mathcal{C}^*(\mathcal{F}(\bar{\mathbf{x}}, \mathbf{w}))) - \mathbf{x}_c(88)$. Contour interval is $5 \times 10^{12} \text{ cm}^3/\text{s}$.

Figure 13: Analysis of the model's observability. The thick curve is the moduli of the coarse, linearized state transition matrix's eigenvalues, and the thin zig-zaggy curve is the norm of the innerproduct of the eigenvectors with the pseudo velocity measurement matrix, \mathbf{H} . The inset figure shows the largest eigenvalues, corresponding to the unstable modes in more detail, of which there are 48.

Figure 14: Sea surface density anomaly of the "model ocean" with velocity data assimilation. (c.i. is 10^{-5} g/cm^3).

Figure 15: Same as Fig 14, except stream function data assimilation.

Figure 16: Same as Fig 14, except density data assimilation.

Figure 17: Root-mean-square errors of the false ocean, e_{false} , as a function of model time; (a) stream function ($10^{13} \text{ cm}^3/\text{s}$), (b) surface zonal velocity (cm/s), (c) density anomaly at mid-collocation depth (10^{-5} g/cm^3). The solid curve is for the present simulation shown in Fig 4, wherein the thin-dashed curve is the errors of the model used by Malanotte-Rizzoli and Young (1992).

Figure 18: Relative root-mean-square error, $e_{\text{assimilation}}/e_{\text{false}}$, for velocity data assimilation as a function of model time. Thick solid curve is for the present approximate Kalman filter while the thin-dashed curve is the result of RY92, with corresponding normalizations (denominators, e_{false}) as shown in Fig 17.

Figure 19: Same as fig 18, except for stream function assimilation.

Figure 20: Same as fig 18, except for density assimilation,

Figure 21: Meridional gradient of absolute vorticity near the center of the channel ($i=65$). (c.i. is $3 \times 10^{-13} (\text{cm s})^{-1}$.)

Figure 22: Normalized error of assimilated model estimate. The figure corresponds to velocity data assimilation. The normalized errors are, $\|(\mathbf{x}_{\text{true}}(t) - \mathbf{x}(t, -))/\mathbf{p}(-)\|$, where $\mathbf{x}_{\text{true}}(t)$ and $\mathbf{x}(t, -)$ are the true value and the assimilated estimate of one of the coarse state variables, respectively, and $\mathbf{p}(-)$ is the corresponding expected error of the estimate. The curves are; barotropic vorticity (ζ , thick solid), zonal (u , thin solid) and meridional (v , thin dash) first baroclinic velocity, barotropic ($p(0)$, thick solid) and first baroclinic ($p(1)$, thick dash) density.

Figure 23: Pseudo altimetry tracks. The pattern of sea level measurements is alternated between the crosses and the diamonds every two days. There are a total of 130 measurement points for each observation pattern,

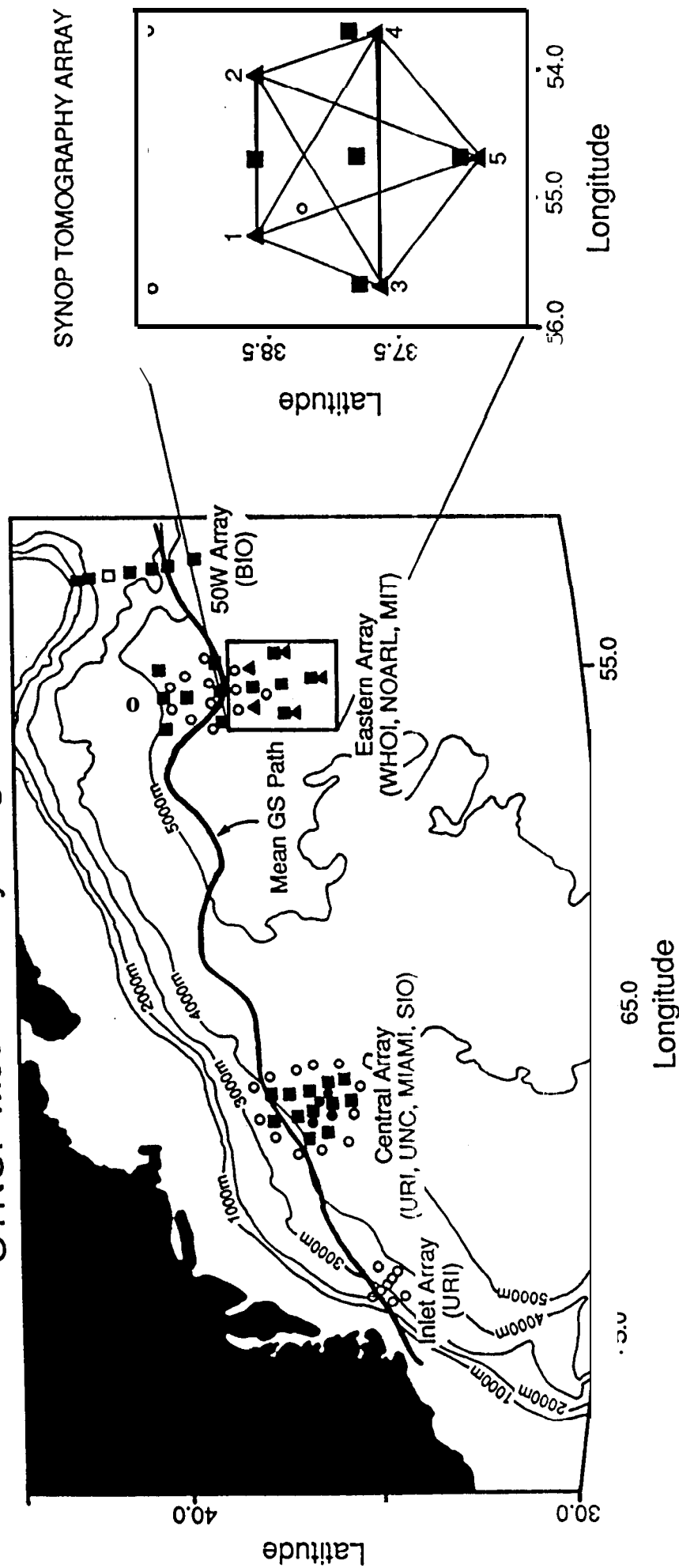
Figure 24: Sea surface density anomaly as in Fig 14, except for pseudo altimetry assimilation.

Figure 25: Relative root-mean-square errors, $e_{\text{assimilation}}/e_{\text{false}}$, for assimilating pseudo altimetry (thick-solid) and pseudo reciprocal tomography (thin-solid).

Figure 26: Pseudo reciprocal tomography array. The source/receiver shown in circles are a subarray of pseudo current meters used in section 3.3. The solid lines show the ray paths along which mean velocities are measured.

Figure 27: Sea surface density anomaly as in Fig 14, except for pseudo reciprocal acoustic tomography assimilation.

SYNOP Moored Array Program



URI..... University of Rhode Island
 BIO..... Bedford Institute of Oceanography
 MIT..... Massachusetts Institute of Oceanography
 NOAARL... Naval Oceanographic and Atmospheric Research Laboratory
 UNC..... University of North Carolina
 SIO..... Scripps Institute of Oceanography
 WHOI... Woods Hole Oceanographic Institute

Fig 1

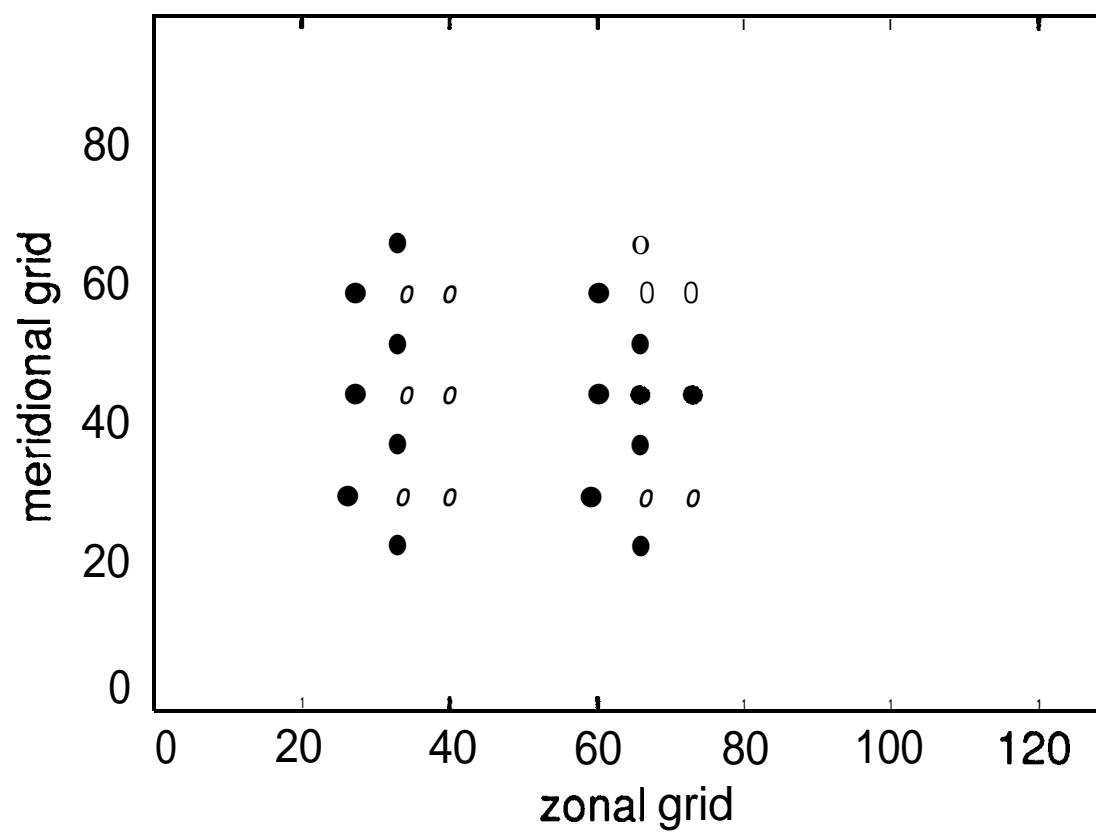
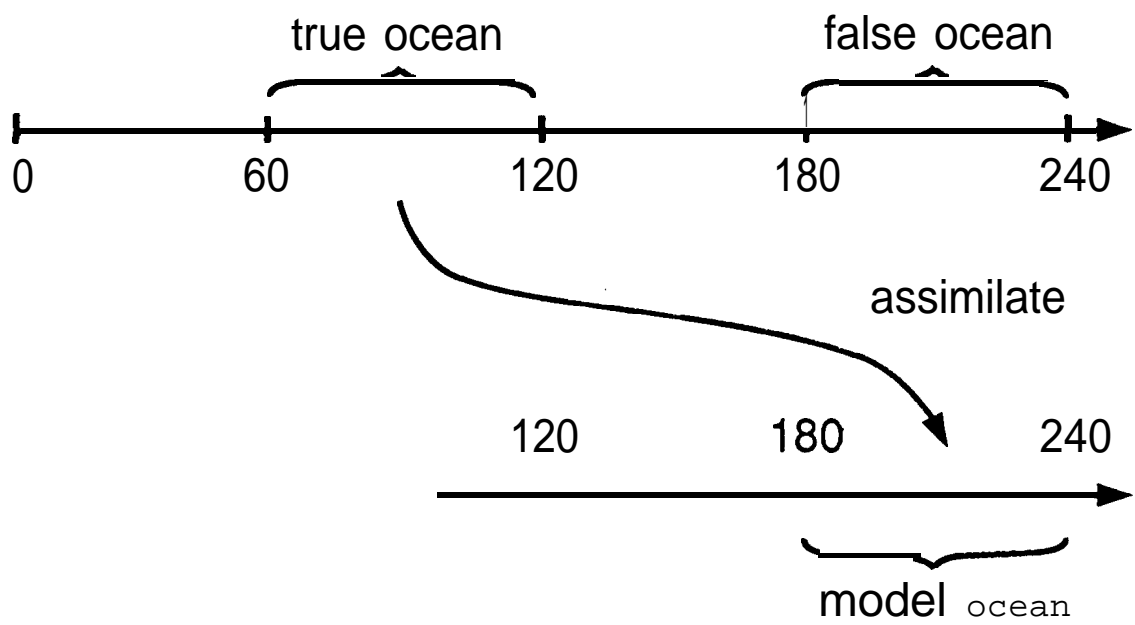


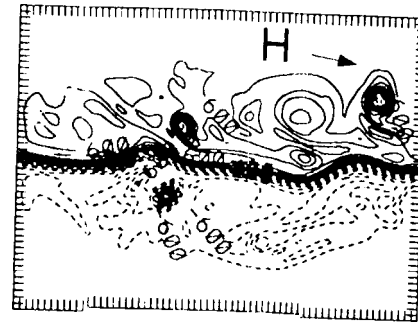
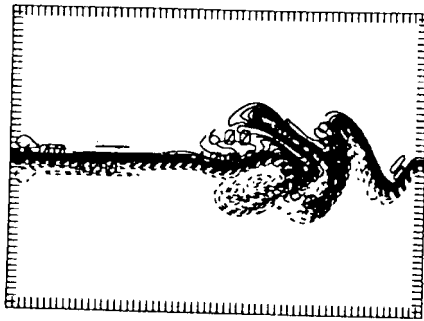
FIG 2



(a) true ocean

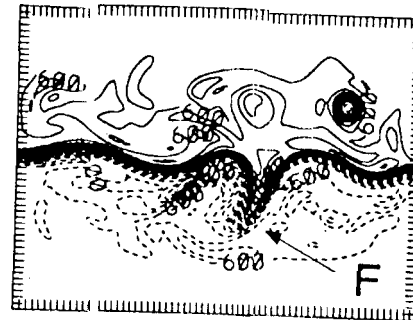
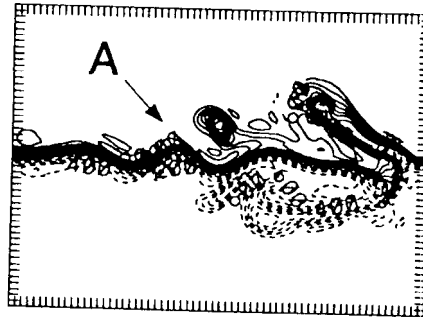
(b) false ocean

t=60



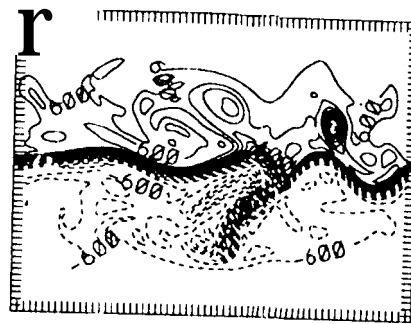
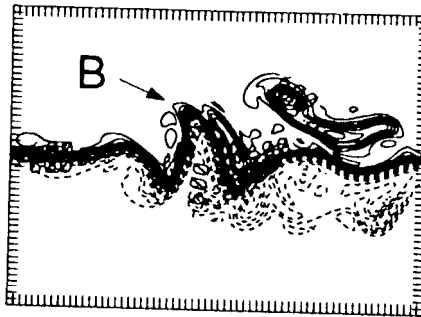
t= 180

t=82



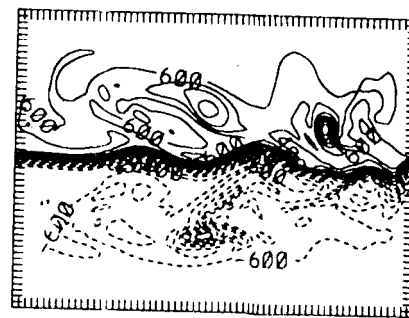
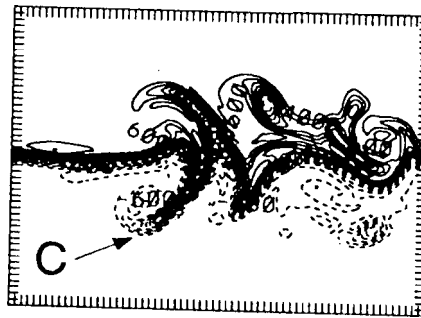
t = 202

t=94



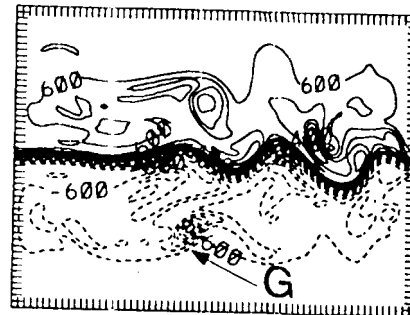
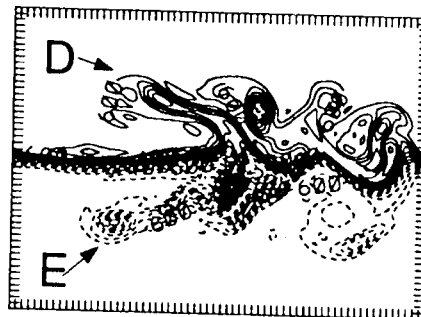
t = 214

t = 106



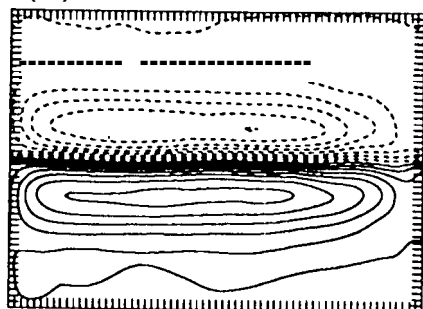
t = 226

t = 118



t = 238

(a) stream function



(b) surface density



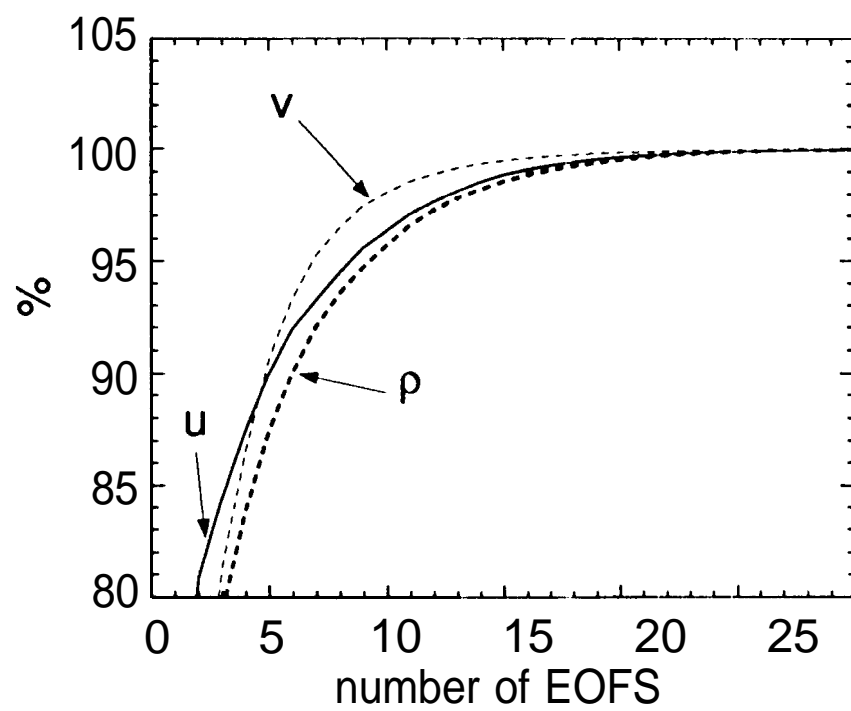


Fig 6

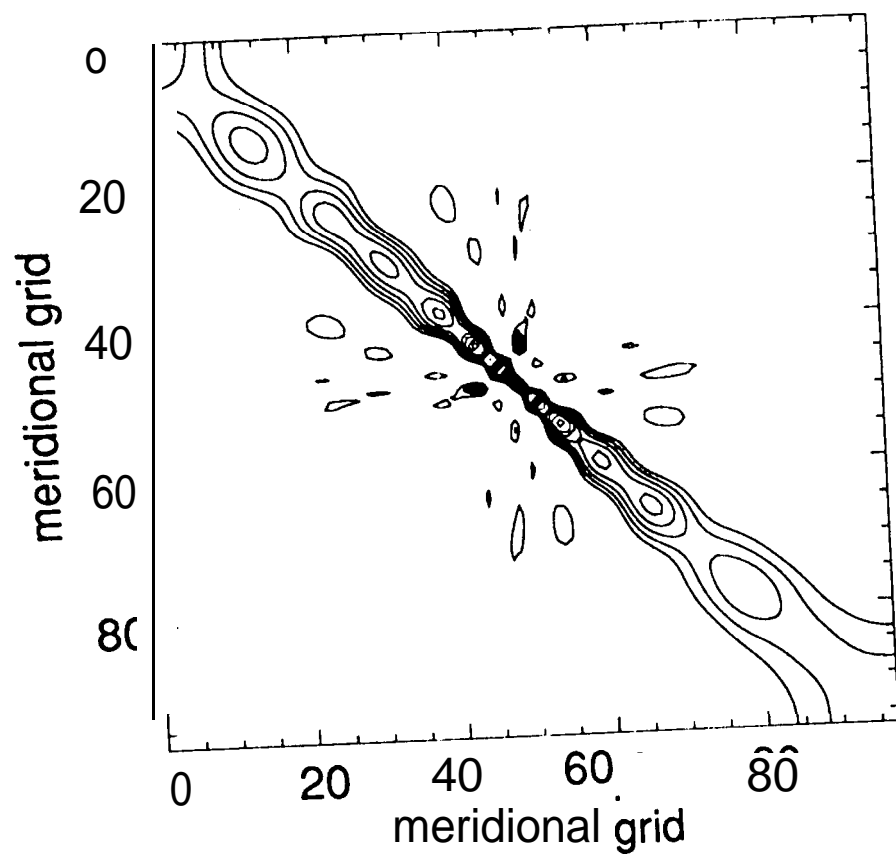
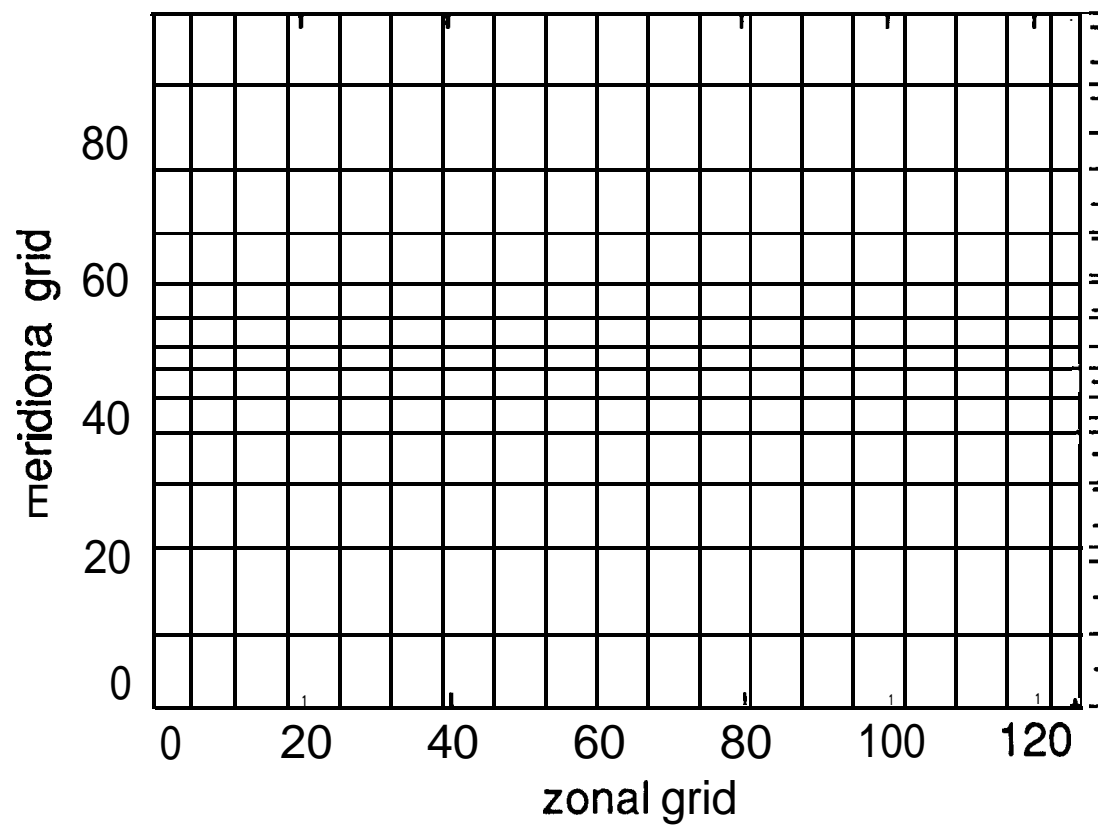


Fig 1



Fg 8

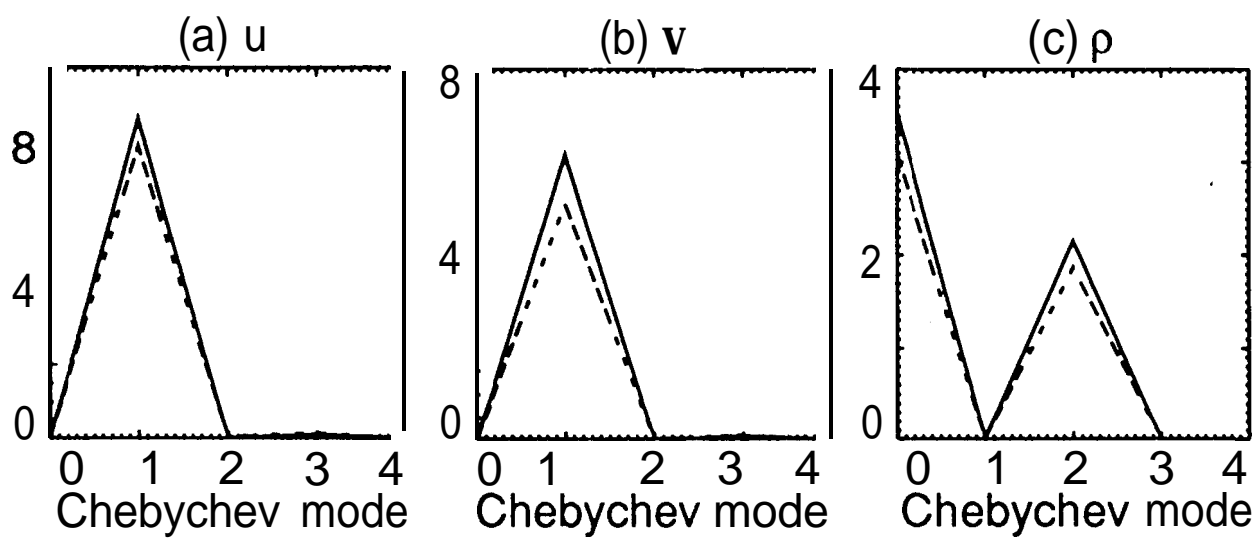
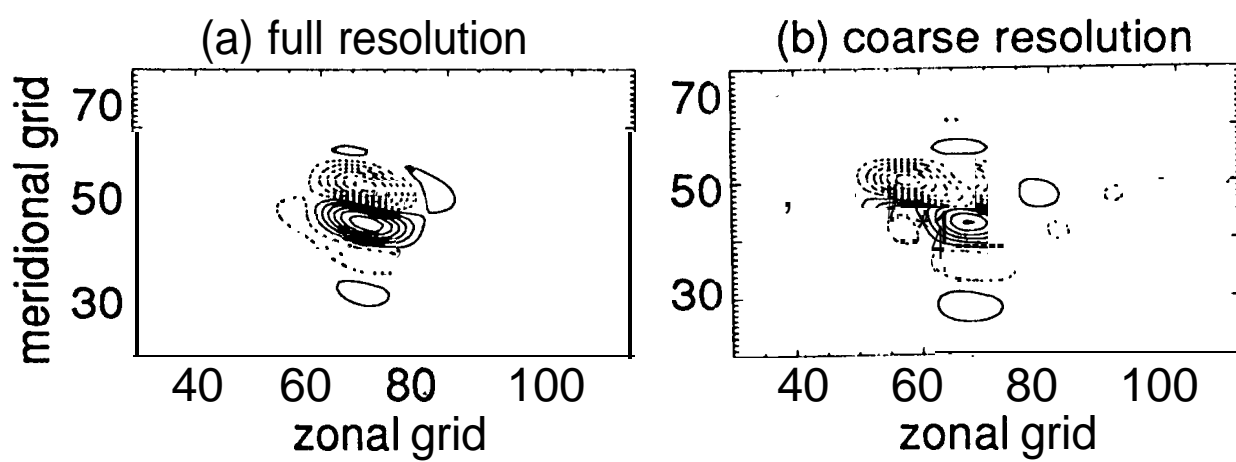
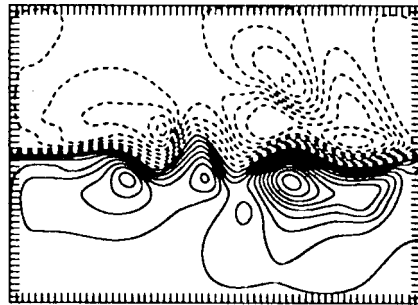


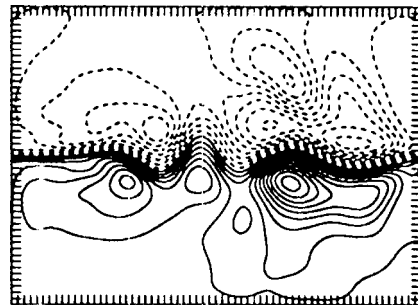
Fig. 9



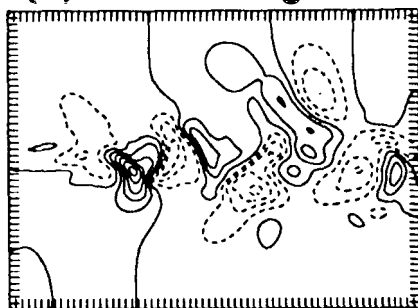
(a) full resolution



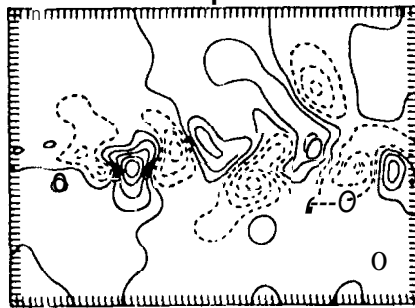
(b) coarse approximation



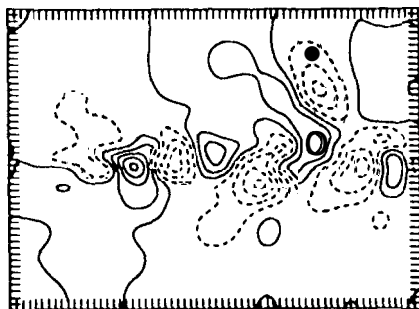
(a) true change



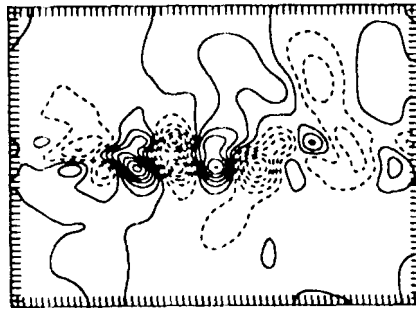
(b) coarse representation



(c) coarse model



(d) linear coarse model



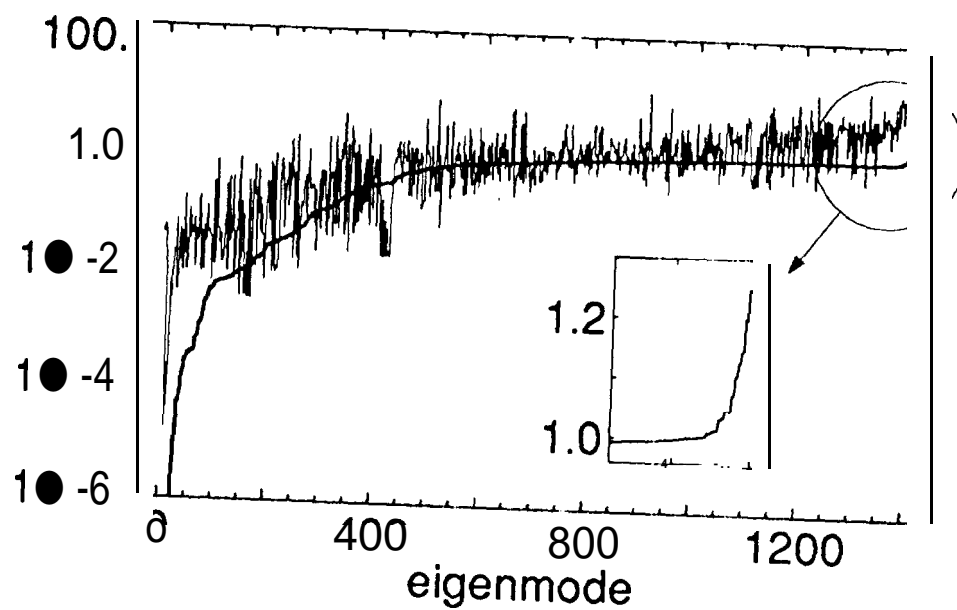
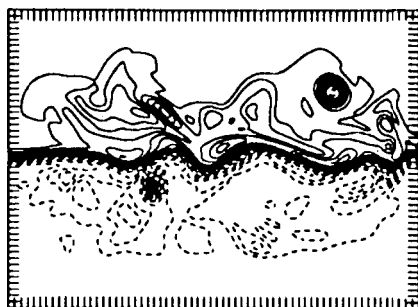
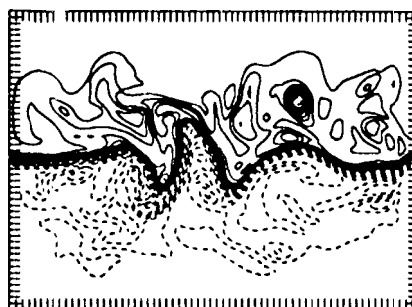


Fig. 13

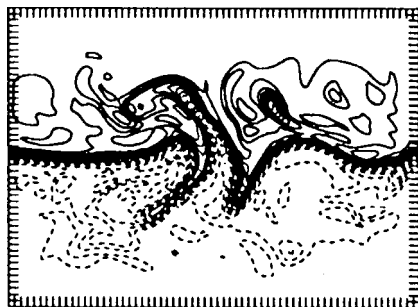
(a) $t = 202$



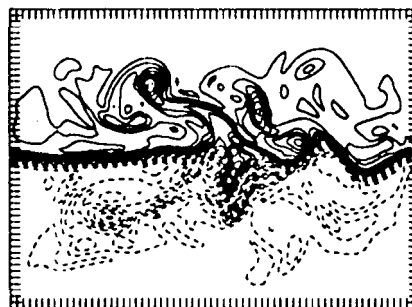
(b) $t = 214$



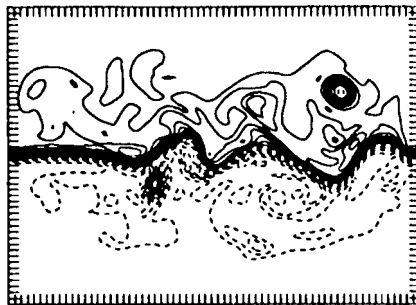
(c) $t = 226$



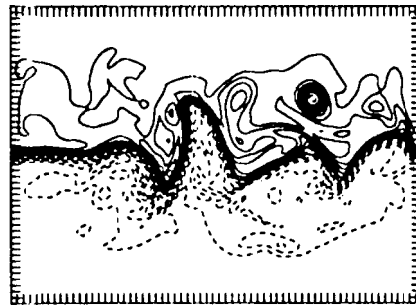
(d) $t = 238$



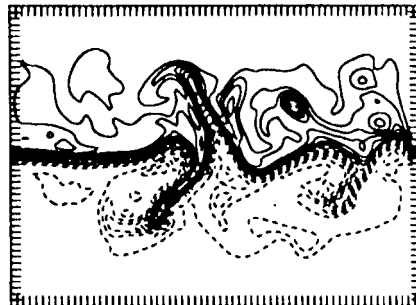
(a) $t = 202$



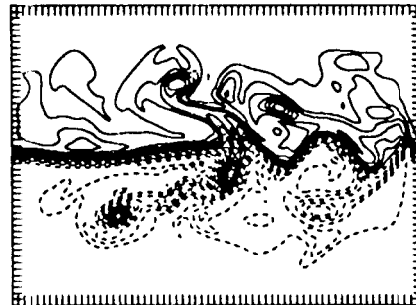
(b) $t = 214$



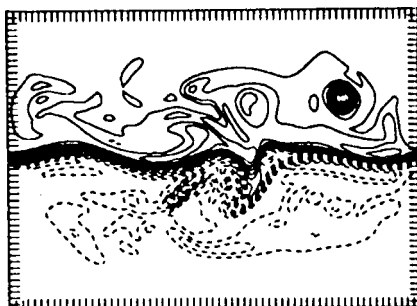
(c) $t = 226$



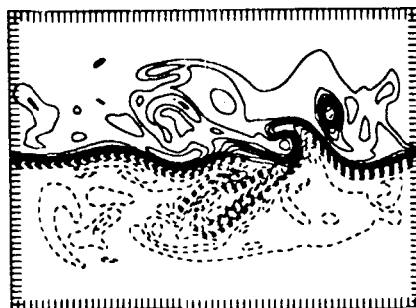
(d) $t = 238$



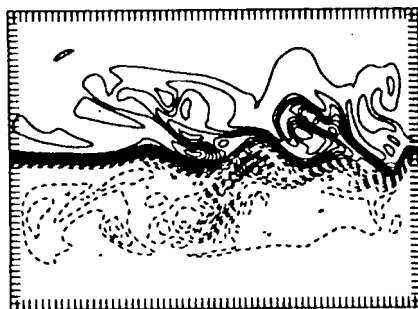
(a) $t = 202$



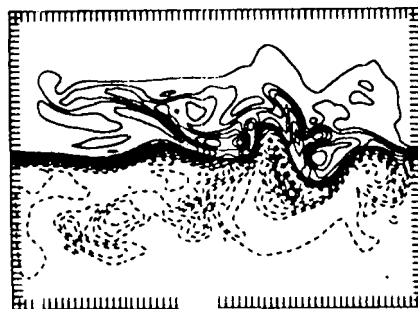
(b) $t = 214$



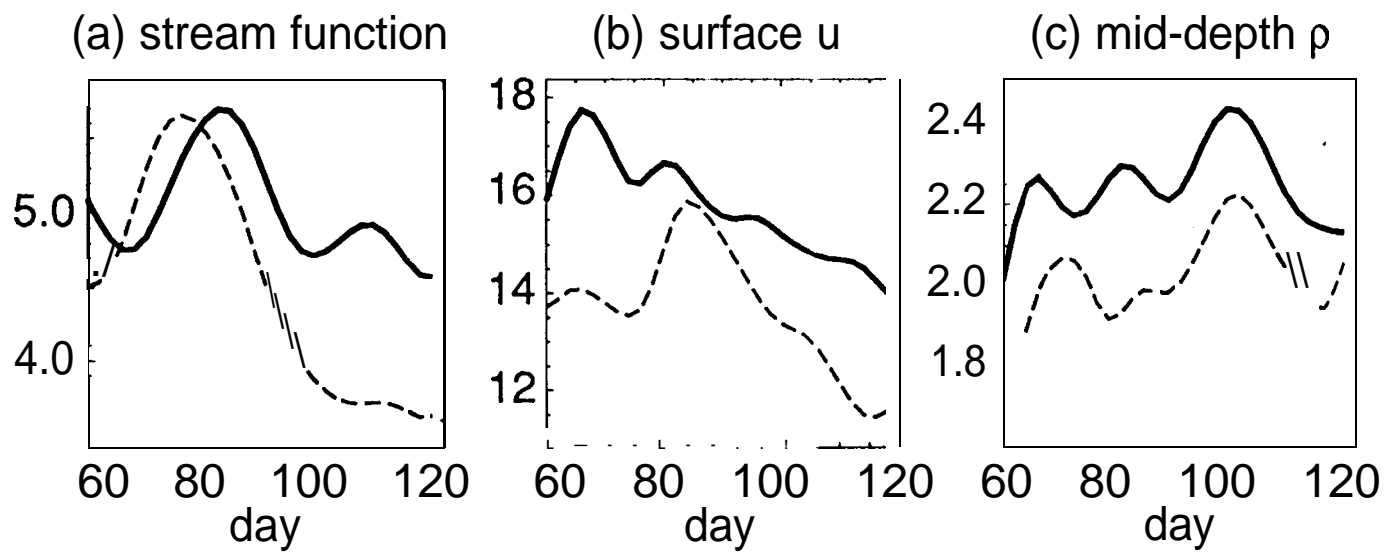
(c) $t = 226$



(d) $t = 238$







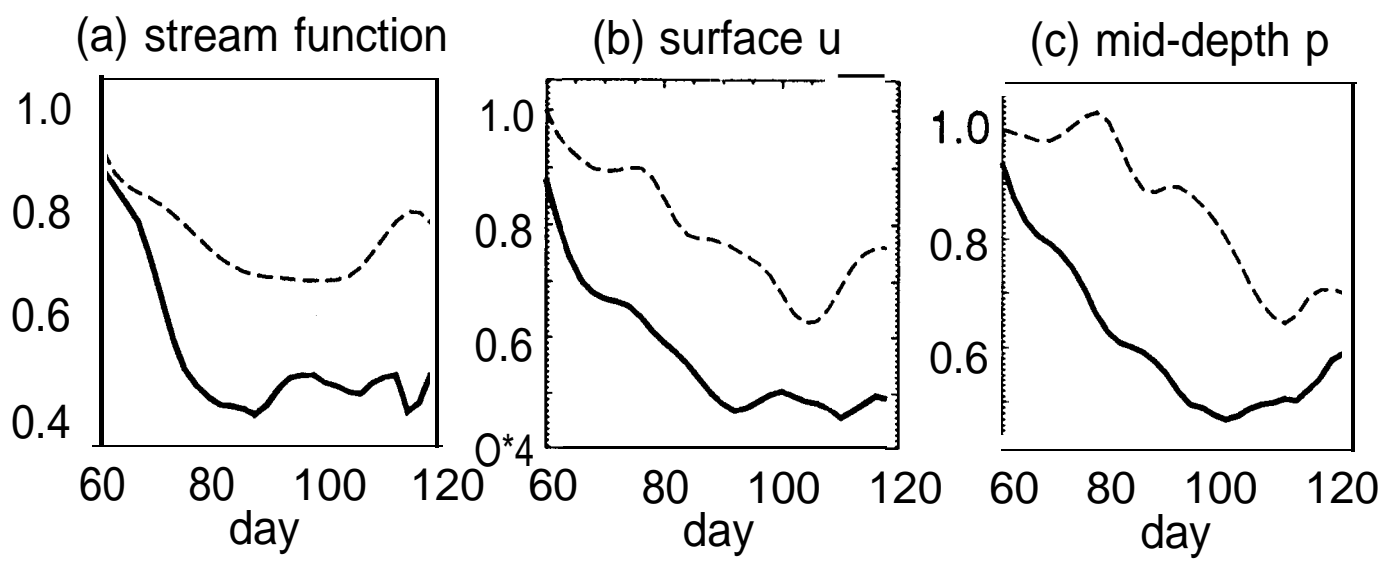
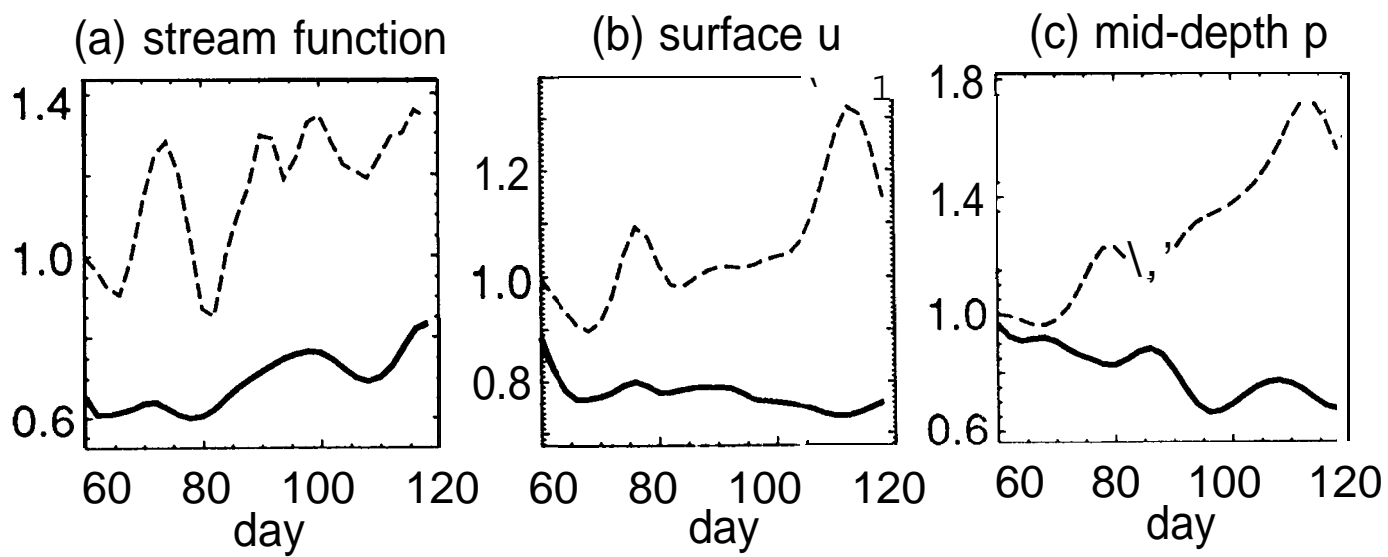


Fig. 18



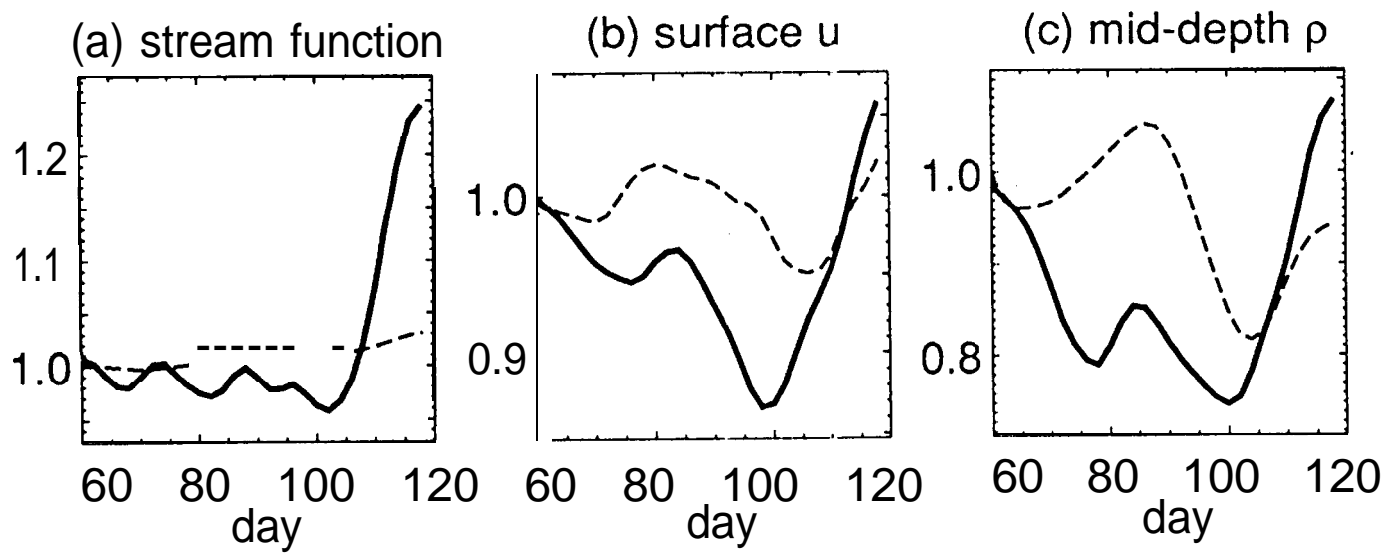


Fig. 20

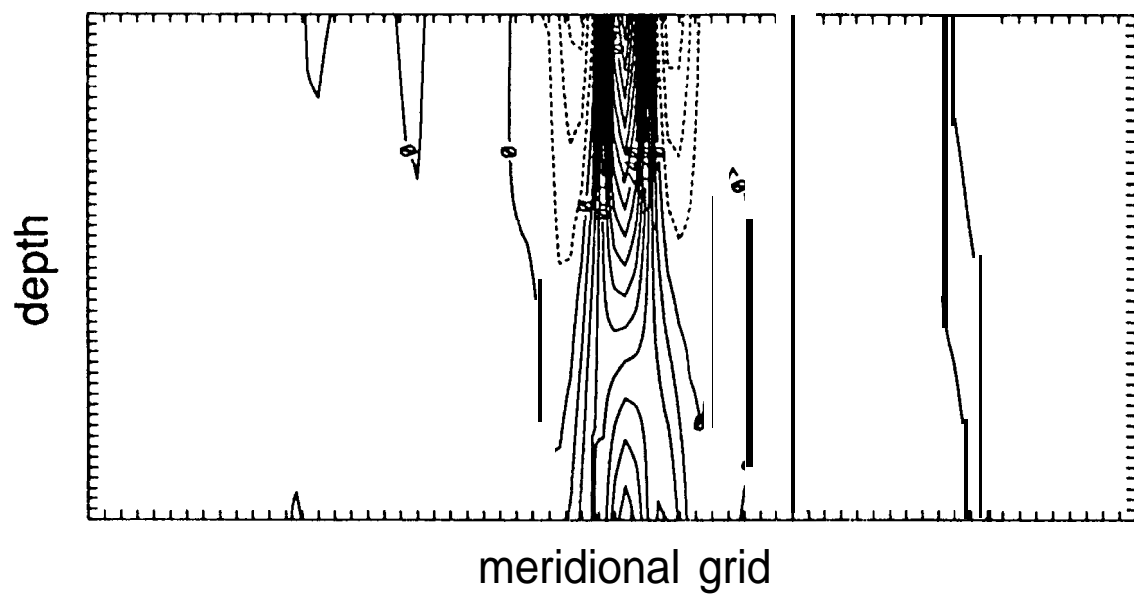


Fig. 21

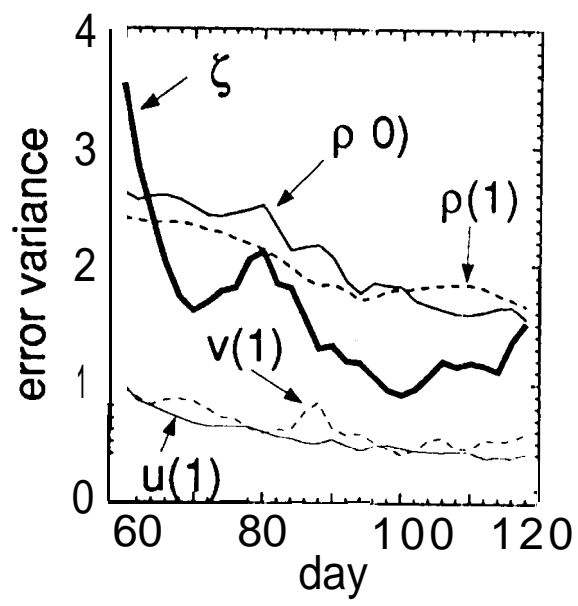


Fig. 22

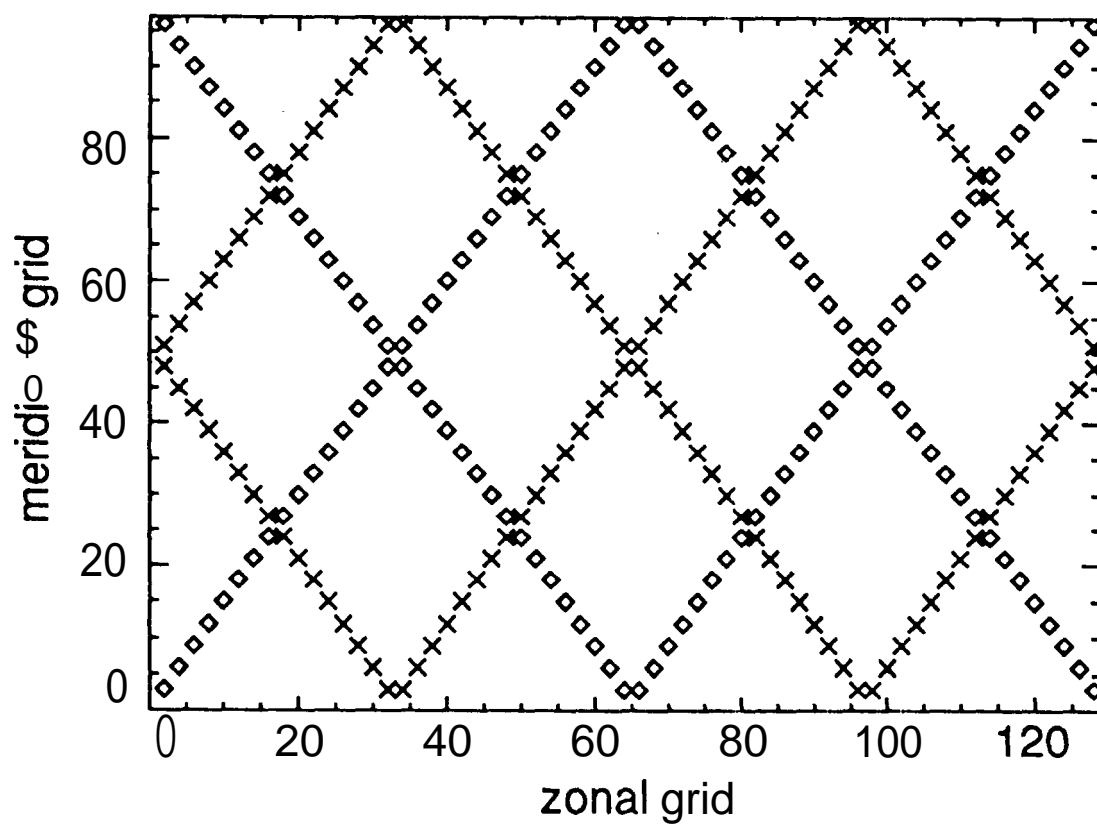
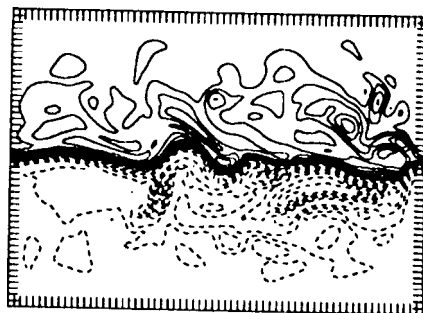
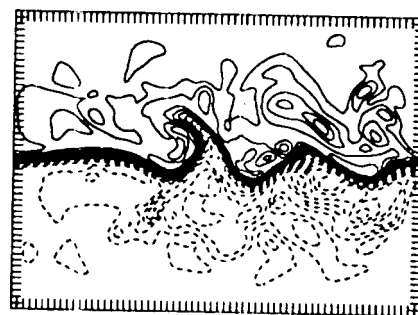


Fig. 23

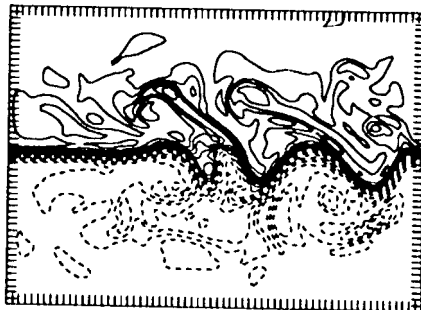
(a) $t = 202$



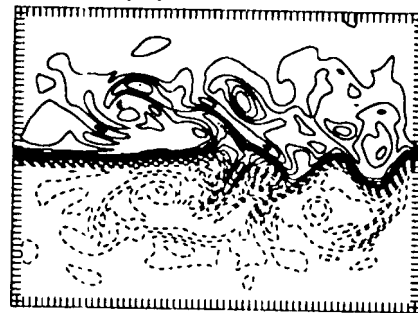
(b) $t = 214$

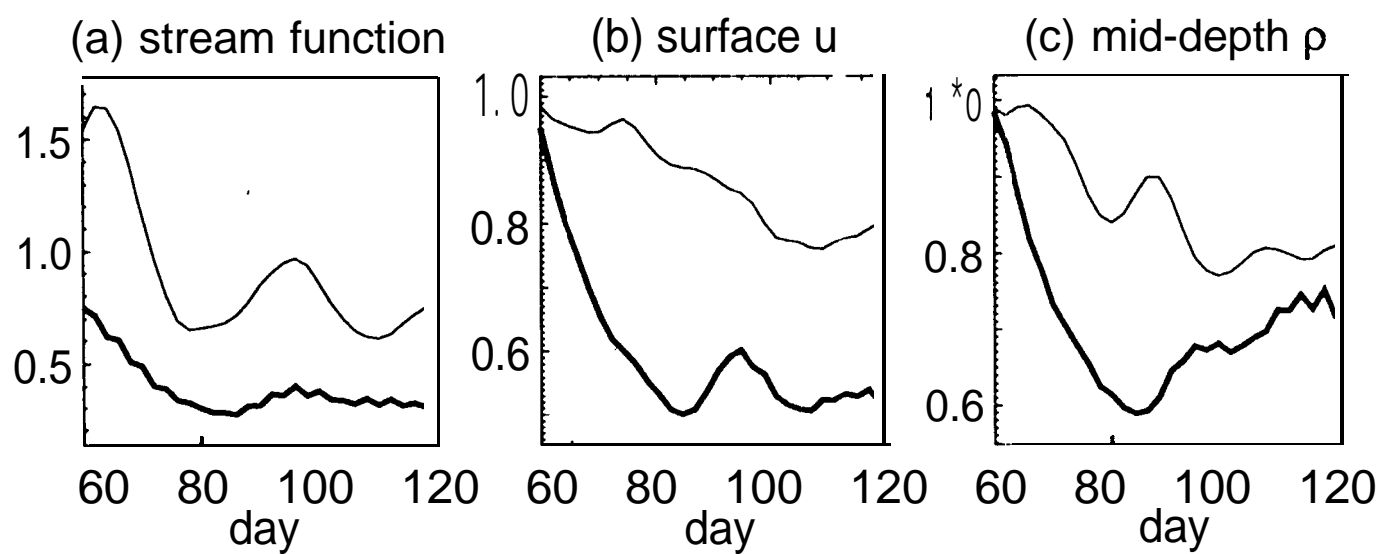


(c) $t = 226$



(d) $t = 238$





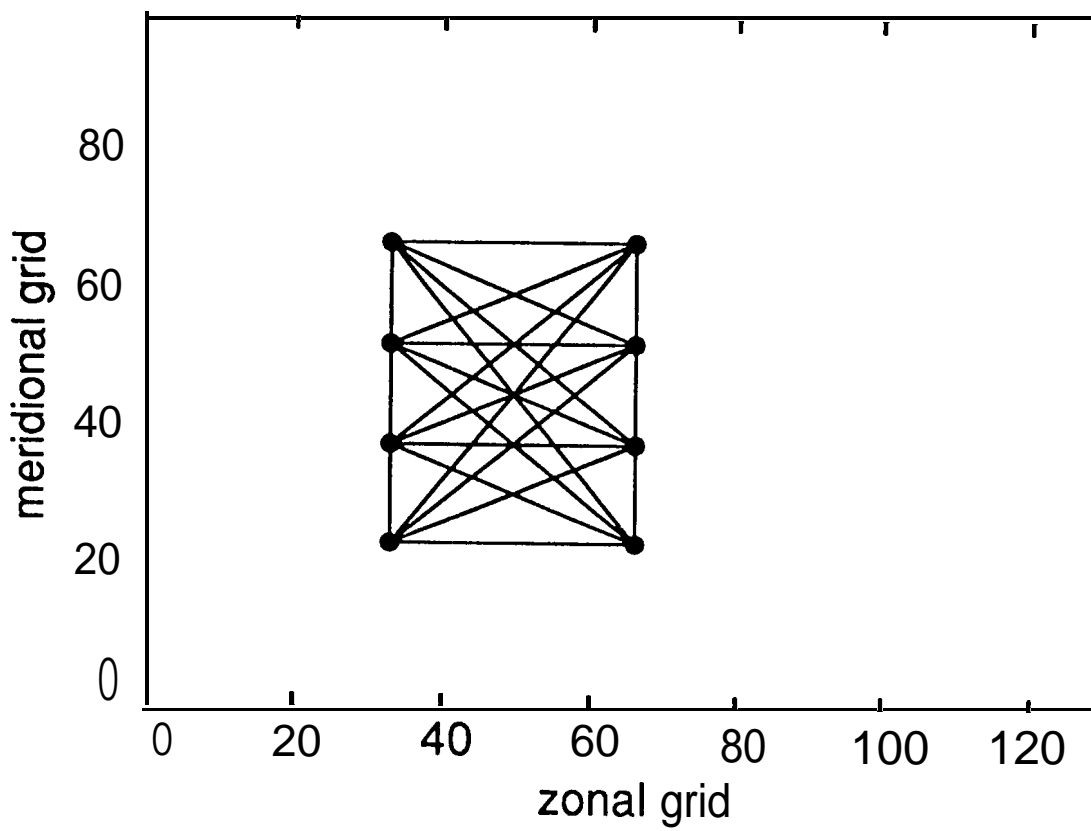
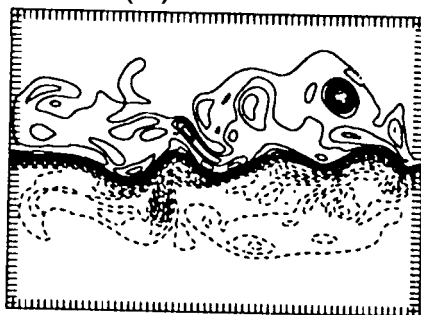
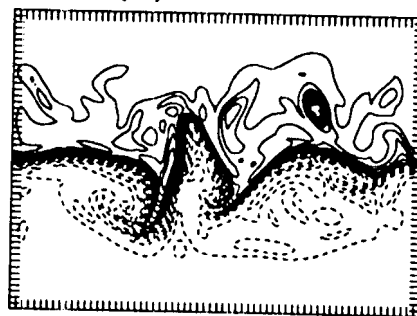


Fig. 2b

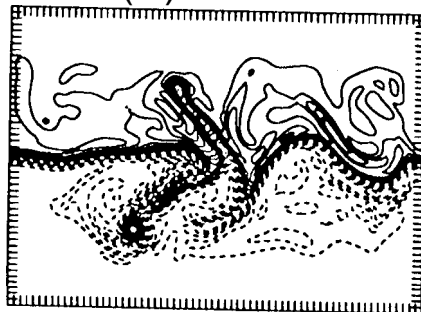
(a) $t = 202$



(b) $t = 214$



(c) $t = 226$



(d) $t = 238$

